Astronomy
&
Astrophysics

# VEGAS: a VST Early-type GAlaxy Survey

## V. IC 1459 group: Mass assembly history in low-density environments

Enrichetta Iodice[1,2], Marilena Spavone[1], Arianna Cattapan[1], Elena Bannikova[3,4], Duncan A. Forbes[5],
Roberto Rampazzo[6], Stefano Ciroi[7,8], Enrico Maria Corsini[7,8], Giuseppe D'Ago[9], Tom Oosterloo[10,11],
Pietro Schipani[1], and Massimo Capaccioli[12]

[1] INAF – Astronomical Observatory of Capodimonte, Salita Moiariello 16, 80131 Naples, Italy
   e-mail: enrichetta.iodice@inaf.it
[2] European Southern Observatory, Karl-Schwarzschild-Strasse 2, 85748 Garching bei Muenchen, Germany
[3] Institute of Radio Astronomy of National Academy of Sciences of Ukraine, Mystetstv 4, 61022 Kharkiv, Ukraine
[4] V.N. Karazin Kharkiv National University, Svobody Sq. 4, 61022 Kharkiv, Ukraine
[5] Centre for Astrophysics and Supercomputing, Swinburne University of Technology, Hawthorn, Victoria 3122, Australia
[6] INAF – Astronomical Observatory of Padova, Via dell'Osservatorio 8, 36012 Asiago, VI, Italy
[7] Department of Physics and Astronomy "G. Galilei", University of Padova, Vicolo dell'Osservatorio 3, 35122 Padova, Italy
[8] INAF – Osservatorio Astronomico di Padova, Vicolo dell'Osservatorio 5, 35122 Padova, Italy
[9] Instituto de Astrofísica, Facultad de Física, Pontificia Universidad Católica de Chile, Av. Vicuña Mackenna 4860, 7820436 Macul,
   Santiago, Chile
[10] ASTRON, Netherlands Institute for Radio Astronomy, Postbus 2, 7990 AA Dwingeloo, The Netherlands
[11] Kapteyn Astronomical Institute, University of Groningen, Postbus 800, 9700 AV Groningen, The Netherlands
[12] University of Naples Federico II, C.U. Monte Sant'Angelo, Via Cinthia, 80126 Naples, Italy

**ABSTRACT**

*Context.* This paper is based on the multi-band VST Early-type GAlaxy Survey (VEGAS) with the VLT Survey Telescope (VST).
We present new deep photometry of the IC 1459 group in $g$ and $r$ band.
*Aims.* The main goal of this work is to investigate the photometric properties of the IC 1459 group, and to compare our results with
those obtained for other galaxy groups studied in VEGAS, in order to provide an initial view of the variation of their properties as a
function of the evolution of the system.
*Methods.* For all galaxies in the IC 1459 group, we fit isophotes and extract the azimuthally averaged surface-brightness profiles, the
position angle, and ellipticity profiles as a function of the semi-major axis. We also extract the average colour profile. In each band,
we estimate the total magnitude, effective radius, mean colour, and total stellar mass for each galaxy in the group. We then look at the
structure of the brightest galaxies and the faint features in their outskirts, considering also the intragroup component.
*Results.* The wide field of view, long integration time, high angular resolution, and arcsec-level seeing of OmegaCAM at VST allow
us to map the light distribution of IC 1459 down to a surface brightness level of 29.26 mag arcsec$^{-2}$ in $g$ band and 28.85 mag arcsec$^{-2}$
in $r$ band, and out to $7-10 R_e$, and to detect the optical counterpart of HI gas around IC 1459. We also carry out an in-depth exploration
of three low-density environments and provide information to understand how galaxy and group properties change with the group
evolution stage.
*Conclusions.* Good agreement is found between our results and predictions of numerical simulations regarding the structural proper-
ties of the brightest galaxies of the groups. We suggest that the structure of the outer envelope of he brightest cluster galaxies (i.e. the
signatures of past mergers and tidal interactions), the intra-group light, and the HI amount and distribution may be used as indicators
of the evolutionary stage and mass assembly of galaxy groups.

**Key words.** galaxies: photometry – galaxies: elliptical and lenticular, cD – galaxies: groups: individual: IC 1459 –
galaxies: fundamental parameters

## 1. Introduction

The hierarchical accretion scenario is one of the main prod-
ucts of the $\Lambda$CDM model, with structures forming as the
result of merging of smaller elements (De Lucia et al. 2006).
In this framework, in the initial epoch the galaxies lie along
cosmic web filaments. Because of gravity, they then fall into
small galaxy groups, and these low-density environments merge
into galaxy clusters (Rudick et al. 2009; Mihos 2015). Galax-
ies spend a significant part of their evolutionary life in these
small environments, which at present contain more than ~60%

of the galaxies in the Universe (Miles et al. 2004). According
to Bower & Balogh (2004), in the local universe the difference
between groups and clusters of galaxies is based on virial mass:
for a group of galaxies it is in the range $10^{13}-10^{14}\, M_\odot$.

During the infall of galaxy groups to form a cluster, the mate-
rial stripped from galaxy outskirts builds up the intra-group light
(IGL) and intra-cluster light (ICL, Fujita 2004; Willman et al.
2004; Contini et al. 2014; DeMaio et al. 2018). The IGL is the
precursor of the ICL (Mihos 2015). Since ICL, as well as the
IGL, is the fossil record of all past interactions and mergers,
the constant evolution and growth of ICL and IGL over time with

the infalling of galaxies in the potential well of the brightest cluster galaxy (BCG), or of the brightest group galaxy (BGG), suggests that the ICL and the IGL properties should be linked to the evolutionary state of the cluster or group (Mihos 2015). In this process, the mass assembly in the BCG or BGG is still ongoing. The imprint of mass assembly in the BCGs and BGGs resides in the stellar halo. This is an extended, diffuse, and very faint ($\mu_g \geq 26-27$ mag arcsec$^{-2}$) component made of stars stripped from satellite galaxies in the form of streams and tidal tails, with multiple stellar components and complex kinematics (see Duc 2017; Mihos et al. 2017, for reviews). Recent theoretical works provide a detailed set of simulations to reproduce the faint features in the galaxy outskirts at comparable levels of the deep observations (i.e. 29–33 mag arcsec$^{-2}$, Pop et al. 2018; Mancillas et al. 2019). These latter authors carried out a census of the various types of low surface brightness (LSB) features and traced their evolution. According to Mancillas et al. (2019), the tidal tails are thick, elongated structures that emerge from the parent galaxy. Alternatively, the stellar streams are tiny filamentary features that originate from the disruption of low-mass satellites in the galaxy halo. Shells have arc-like concentric shapes and, depending on the nature and projection, they can appear aligned on the same axis. Tidal tails and shells in the galaxy outskirts result from intermediate and major mergers (mass ratio 7:1 to 3:1), whereas the stellar streams are typical signatures of minor mergers. The survival time is estimated to between 0.7 and 4 Gyr, where tidal tails have the shorter lifetime with respect to shells and streams.

Semi-analytic models combined with simulations provide detailed predictions about the structure and stellar populations of stellar halos, the ICL/IGL formation and the amount of substructures in various kinds of environment (Oser et al. 2010; Cooper et al. 2013, 2015; Cook et al. 2016; Pillepich et al. 2018; Monachesi et al. 2019). Predictions cited above suggest that the BCGs and BGGs have an inner stellar component formed in-situ, whereas the accreted ex-situ component contains all the accreted material. The ex-situ component is made by the relaxed component, which is completely merged with the in-situ component, and by the unrelaxed component, which is the outer stellar envelope. Simulations show that in the surface-brightness radial profile of simulated galaxies there is evidence of inflection in the region of the stellar halos, corresponding to variation in the ratio between the accreted relaxed and the accreted unrelaxed components (Cooper et al. 2010; Deason et al. 2013; Amorisco 2017). The distance from the galaxy centre where the inflection occurs is the transition radius ($R_{tr}$) used to characterise a stellar halo. Massive galaxies with a high accreted mass fraction have a small $R_{tr}$ (Cooper et al. 2010, 2013). The unrelaxed component of the stellar envelope appears as a change in the slope of the surface brightness profiles at larger radii. In this context, the study of the surface brightness profiles of BCG and BGG at the faintest levels is potentially one of the main ways to quantify the contribution of the accreted mass, which becomes particularly efficient when the outer stellar envelope starts to be dominant beyond the transition radius (Iodice et al. 2016, 2017a; Spavone et al. 2017a, 2018).

In the last two decades, great improvement of the study of BCGs and BGGs and of the ICL in different types of environment has been afforded by deep imaging surveys aimed at studying galaxy structures out to regions where the galaxy light merges into the intra-cluster component (Ferrarese et al. 2012; van Dokkum et al. 2014; Duc et al. 2015; Muñoz et al. 2015; Merritt et al. 2016; Mihos et al. 2017). The VST Early-type

GAlaxy Survey (VEGAS[1], Capaccioli et al. 2015) has played a pivotal role in this field in recent years. VEGAS is a multi-band *ugri* imaging survey with the VLT Survey Telescope (VST). Taking advantage of the large field of view of OmegaCAM at VST, VEGAS data allow us to relate galaxy structure to environment, from the dense cluster of galaxies (see Iodice et al. 2019, and reference therein) to the unexplored poor groups of galaxies (Spavone et al. 2018; Cattapan et al. 2019). With the VEGAS data we are able to map the surface brightness of galaxies down to $\mu_g \sim 30$ mag arcsec$^{-2}$ and out to about $10R_e$ (Spavone et al. 2017a; Iodice et al. 2019). The deep photometry allows us to trace the mass assembly in galaxies, by estimating the accreted mass fraction in the stellar halos, detecting the ICL and the stellar streams in the intra-cluster space, and providing results that can be directly compared with the predictions of galaxy formation models (Iodice et al. 2016, 2017b,a; Spavone et al. 2017a, 2018; Cattapan et al. 2019). Recently, in the deep imaging data of VEGAS for the NGC 5846 group of galaxies, we were able to detect an ultra diffuse galaxy, with an absolute magnitude of $M_g = -14.2$ mag, corresponding to a stellar mass of $\sim 10^8 \, M_\odot$ (Forbes et al. 2019).

In this work we present a new VEGAS deep mosaic of $1 \times 2$ square degrees of the group of galaxies centred on the BGG IC 1459. We use *g*, *r*, and *i* images to analyse the structure of the group members in order to look for LSB features in the BGG outskirts and in the intra-group space. Results are compared with those obtained for another two galaxy groups studied in VEGAS, the NGC 5018 group (Spavone et al. 2018) and the NGC 1533 triplet (Cattapan et al. 2019), since data have comparable depth and were analysed using the same methods and tools.

The paper is organised as follows. In Sect. 2 we describe the IC 1459 group and its main properties. The observing strategy and the data-reduction procedure are reported in Sect. 3. In Sect. 4 we present the data analysis and in Sect. 5 we describe the results for the IC 1459 group. In Sect. 6 we compare the results of the three analysed VEGAS groups with theoretical predictions and with previous observational results. In Sect. 7 we draw our conclusions.

## 2. The IC 1459 group

The IC 1459 group (also known as LGG 466) hosts nine bright galaxies, of which seven are late-type galaxies (LTGs, Brough et al. 2006). IC 1459 is an early-type galaxy (ETG) located in the group projected centre and is considered to be the BGG (Saponara et al. 2018). By adopting the virial radius given by Brough et al. (2006) of $r_{200} = 0.21$ Mpc, we derived the virial mass for the group: $M_{200} \simeq 3.7 \times 10^{13} \, M_\odot$. Here, we study the brightest galaxies in the range of magnitudes $-23 \leq M_g \leq 19.6$ mag. IC 1459 is one of the two ETGs of the group; it is the most massive, $\mathcal{M}_{tot}^* = 1.0 \times 10^{12} \, M_\odot$, and luminous, $L_{tot,g} = 1.77 \times 10^{11} \, L_\odot$. Table 1 lists the main properties of the galaxies in the IC 1459 group and Fig. 1 shows the OmegaCAM at VST mosaic in *g* band of the group. We consider each of the group members at the same distance as IC 1459, that is $D = 28.70$ Mpc, based on the HI data (Brough et al. 2006; Serra et al. 2015; Saponara et al. 2018; Oosterloo et al. 2018).

In recent decades, the entire group centred on IC 1459 has been well studied in a wide range if wavelengths. Osmond & Ponman (2004) found X-ray emission from a diffuse intragroup medium. Kilborn et al. (2009), by studying the

---

[1] See http://www.na.astro.it/vegas/VEGAS/Welcome.html

**Table 1.** Basic properties of the galaxies in the IC 1459 group.

| Galaxy | Morphological type | RA (J2000) | Dec (J2000) | Helio-radial velocity (km s$^{-1}$) |
|---|---|---|---|---|
| IC 1459 | E3-4 | $22^h57^m10\overset{s}{.}61$ | $-36°27'44\overset{''}{.}0$ | 1802 |
| IC 5269 | SAB0(rs): | $22^h57^m43\overset{s}{.}66$ | $-36°01'34\overset{''}{.}4$ | 1967 |
| IC 5269B | SB(rs)cd: | $22^h56^m36\overset{s}{.}72$ | $-36°14'59\overset{''}{.}2$ | 1667 |
| IC 5270 | SB(r)cd: (e) | $22^h57^m54\overset{s}{.}94$ | $-35°51'29\overset{''}{.}0$ | 1983 |
| IC 5264 | Sab pec (e)n | $22^h56^m53\overset{s}{.}04$ | $-36°33'15\overset{''}{.}0$ | 1934 |
| ESO 406−27 | SA(rs)d: | $22^h56^m41\overset{s}{.}25$ | $-36°46'21\overset{''}{.}8$ | 2102 |
| NGC 7418 | SAB(rs)cd | $22^h56^m36\overset{s}{.}16$ | $-37°01'48\overset{''}{.}3$ | 1450 |
| NGC 7421 | SB(rs)bc | $22^h56^m54\overset{s}{.}33$ | $-37°20'50\overset{''}{.}1$ | 1792 |
| IC 5273 | SB(rs)cd: | $22^h59^m26\overset{s}{.}70$ | $-37°42'10\overset{''}{.}4$ | 1293 |

**Notes.** Morphological classifications are from RC3, the Third Reference Catalogue of Bright Galaxies (de Vaucouleurs et al. 1991). Coordinates and radial velocities are from NED, the NASA/IPAC Extragalactic Database (https://ned.ipac.caltech.edu).

HI content of the group, pointed out that the gas-rich spirals have typical HI masses, which suggests that the gas removal mechanisms are not yet activated. Therefore, according to the subsequent analysis by Serra et al. (2015), the HI distribution seems to be consistent with a relatively early stage of group assembly. In contrast, the brightest group member IC 1459 shows clear signs of accretion and/or merging events. The first study of the IC 1459 was provided by Malin (1985) using photographic plates. This author pointed out the disturbed morphology in the outskirts in the form of spiral-like features. The morphology of IC 1459 appears quite disturbed by the presence of a dust lane in the centre (Forbes et al. 1994) and by shells, plumes, and faint features in the galaxy outskirts (Forbes et al. 1995). The galaxy hosts an active galactic nucleus with two symmetric radio jets (Tingay & Edwards 2015). Stellar kinematics revealed the existence of a fast counter-rotating stellar core that might result from the accretion of counter-rotating cold gas streams in early times (Franx & Illingworth 1988; Prichard et al. 2019).

## 3. Observations and data reduction

The IC 1459 group is one of the VEGAS targets (P.I. E. Iodice; Capaccioli et al. 2015). VEGAS is a multi-band $u$, $g$, $r$ and $i$ imaging survey obtained with the European Southern Observatory (ESO) Very Large Telescope Survey Telescope (VST). The VST is a 2.6 m wide field optical telescope (Schipani et al. 2012) equipped with OmegaCAM, a $1° \times 1°$ camera with a resolution of 0.21 arcsec pixel$^{-1}$. The data we present were obtained in visitor mode (run IDs: 097.B-0806(B), 098.B-0208(A) and 0100.B-0168(A)) in dark time. The total integration times and the average FWHM in each band are given in Table 2. A detailed description of the data reduction, which uses the dedicated pipelines developed to process Omega-Cam observations (VST-Tube and AstroWISE), is provided by McFarland et al. (2013), Grado et al. (2012), Capaccioli et al. (2015), Spavone et al. (2017b), Venhola et al. (2018).

For the IC 1459 group, we obtained a mosaic of about $1° \times 2°$ (Fig. 1). Data were acquired with the step dither observing strategy, which consists of a cycle of short exposures (~150 s) on the science target and on an adjacent field (close in space and time) to the science frame. This strategy was adopted for other VEGAS targets (e.g. the NGC 5018 group; Spavone et al. 2018) and for the Fornax Deep Survey (FDS; Iodice et al. 2016; Venhola et al. 2018) and guarantees a very accurate estimate of the sky background because an average sky frame is derived

for each observing night and then subtracted from each science frame. With the total exposure times adopted for the observations of the IC 1459 group, the obtained surface brightness depths for a point source at $5\sigma$ over an area of $FWHM = 1.26$ arcsec are $\mu_g = 27.3$ mag, $\mu_r = 28.9$ mag, and $\mu_i = 26.2$ mag in the $g$, $r$, and $i$ bands, respectively.

By adopting the same method for the sky-subtracted and stacked images as that described in Iodice et al. (2016), we estimated any residual fluctuations[2] and the limiting radius from the galaxy centre where the galaxy's light blends into the background. In short, for each galaxy of the sample and in each band, we extracted the azimuthally averaged intensity profile (using the IRAF task ELLIPSE) on the sky-subtracted mosaic, after masking all the bright sources (galaxies and stars) and background objects, and from it we estimated the outermost radius, from the centre of the galaxy, where counts are consistent with the average background level. Such a value is the residual by the subtraction of the sky frame, and therefore is very close to zero. The limiting radius sets the surface brightness limit of the VST light profiles and gives an estimate on the accuracy of the sky subtraction. The fluctuations of the background level are on average in the range 0.6–1 counts in the $g$ and $r$ bands, respectively, and close to zero counts in the $i$ band. The rms in the background fluctuations, which quantifies the quality of the sky subtraction, is in the range 0.04–0.06 counts. The rms and the uncertainties on the photometric calibration (~0.003–0.006 mag) are taken into account when computing the total uncertainty on the surface brightness magnitudes[3]. For IC 1459, the limiting radius is 20 arcmin (~167 kpc) in the $g$ and $r$ bands, and 10 arcmin (~83 kpc) in the $i$ band. At these radii, we map the surface brightness down to $\mu = 29 \pm 1$ mag arcsec$^{-2}$ in the $g$ and $r$ bands.

To fully account for the broadening effect of the seeing on the light distribution of galaxies, Capaccioli et al. (2015)

---

[2] The "residual fluctuations" in the sky-subtracted images are the deviations from the background in the science frame with respect to the average sky frame obtained by the empty fields close to the target. Therefore, by estimating them, we obtain an estimate on the accuracy of the sky-subtraction step.

[3] The uncertainty in the surface brightness is calculated with the following formula: $\text{err} = \sqrt{(2.5/(\text{adu} \times \ln(10)))^2 \times ((\text{err}_{adu} + \text{err}_{sky})^2) + \text{err}_{zp}^2}$, where $\text{err}_{adu} = \sqrt{\text{adu}/N - 1}$, and $N$ is the number of pixels used in the fit, $\text{err}_{sky}$ is the rms on the sky background, and $\text{err}_{zp}$ is the error on the photometric calibration (Capaccioli et al. 2015; Seigar et al. 2007).
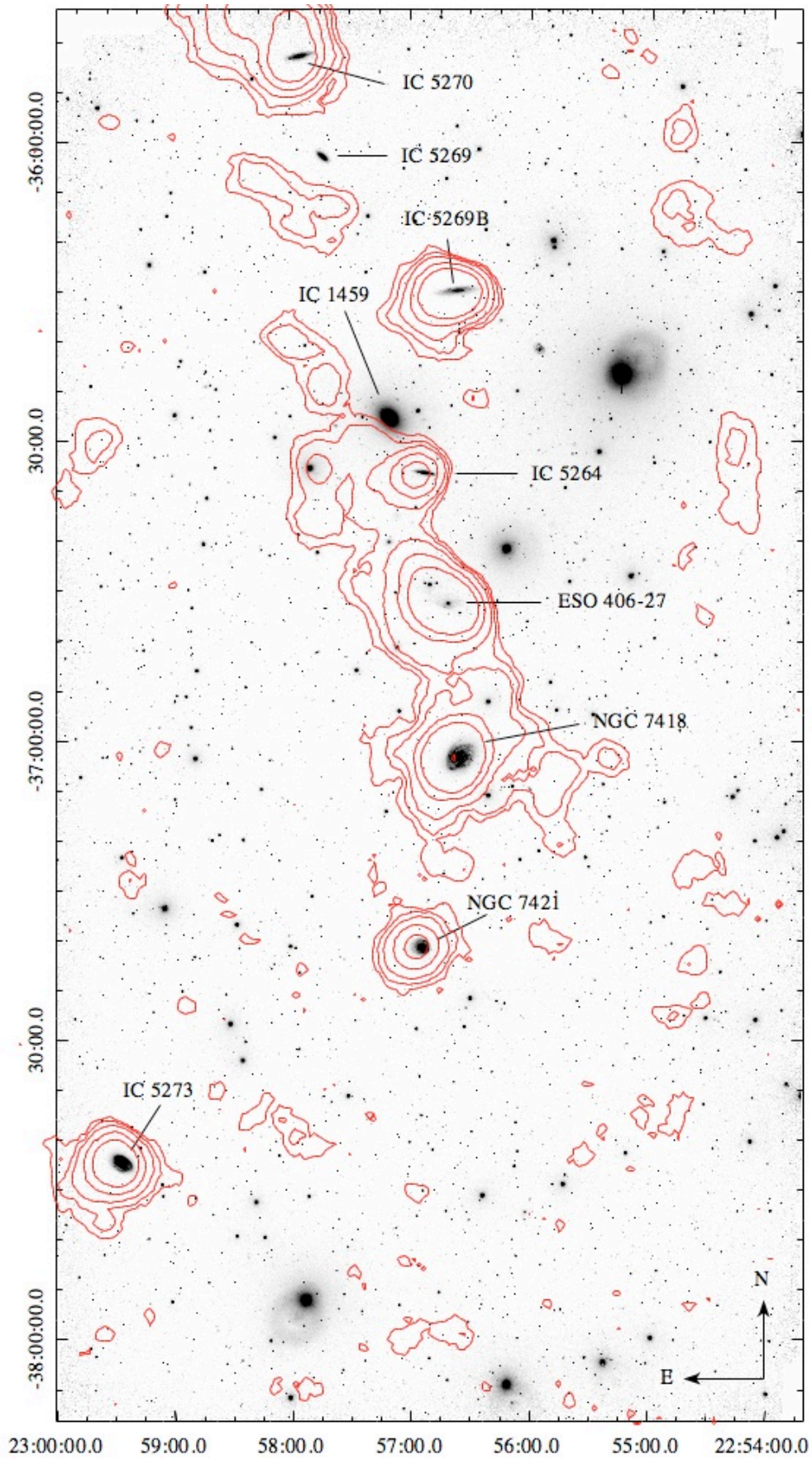
**Fig. 1.** OmegaCAM at VST mosaic in $g$ band of the IC 1459 group with the HI map from the KAT−7 observations (red contours). The image size is about $1° \times 2°$, and the HI contour levels are 5.5, 10, 20, 50, and $100 \times 10^{18}$ cm$^{-2}$ (as shown by Oosterloo et al. 2018). The right ascension and declination (J2000) are given in the horizontal and vertical axis of the field of view, respectively. North is at the top and east is to the left.

**Table 2.** Observation log.

| Band (1) | RA (J2000) (2) | Dec (J2000) (3) | $T_{exp}$ (s) (4) | *FWHM* (arcsec) (5) |
|------|------|------|------|------|
| $g$ | $22^h56^m51\overset{s}{.}36$ | $-37°00'50\overset{''}{.}4$ | 14250 | 1.73 |
| $r$ | $22^h56^m51\overset{s}{.}36$ | $-37°00'50\overset{''}{.}4$ | 14400 | 0.89 |
| $i$ | $22^h56^m51\overset{s}{.}36$ | $-37°00'50\overset{''}{.}4$ | 12750 | 0.94 |

**Notes.** Column 1: filters in the SDSS band; Cols. 2 and 3: central right ascension and declination of the mosaic; Col. 4: total exposure time; Col. 5: median value of the seeing, FWHM, of the combined frames.

characterised the point spread function (PSF) for VST by using stars on the acquired VST images. These latter authors provided the global PSF surface brightness profile, which takes into account the scattered light out to a radial distance comparable to that of the major axis diameter of the galaxies (see Fig. B.1 in Capaccioli et al. 2015). Where needed, a two-dimensional model of the bright stars, close in projection to the galaxy under study, is derived and subtracted from the image before performing the analysis of the light distribution (see also Sect. 4).

# 4. Data analysis

In this section we describe the analysis performed on the new VEGAS data for the IC 1459 group. We provide a detailed description of the galaxy structure at the new faintest surface brightness levels, focusing on the outskirts of the BGG IC 1459. In addition, we derive the (i) light profiles in all bands and colour distribution for all galaxies of the group; (ii) the contribution to the light of the different components in the BGG; and (iii) the intra-group light. Taking advantage of the deep imaging from VEGAS, the main science goal of this analysis is to address the mass assembly history of the IC 1459 group (see Sect. 5).

## 4.1. The low-surface-brightness features in IC 1459 groups

In Fig. 2 we show an enlarged region of the VST mosaic around IC 1459 in the $g$-band surface brightness levels[4]. This is the region of the group where the majority of the faint low-surface-brightness features are detected. All of them are in the outskirts of the brightest group member IC 1459. The galaxy shows an extended ($\simeq 8$ arcmin) envelope down to $\mu_g \sim 27\,\mathrm{mag\,arcsec^{-2}}$, which appears twisted with respect to the central brightest region of the galaxy and very irregular in shape; it is more elongated in the NE–SW direction, where we detect faint ($\mu_g \sim 26.5\,\mathrm{mag\,arcsec^{-2}}$) concentric shells at a distance of $\simeq 5-8$ arcmin from the galaxy centre. In the same range of radii, to the NW, the envelope has prominent sharp edges at the surface brightness levels of $\mu_g \sim 24.5-26.5\,\mathrm{mag\,arcsec^{-2}}$. An elongated thick structure, of $\simeq 10$ arcmin with $\mu_g \sim 26.5\,\mathrm{mag\,arcsec^{-2}}$, extends from east to west in the southern region of the galaxy. Following Mancillas et al. (2019), this resembles a tidal tail.

The small group member IC 5264 (see Fig. 1) in the SW region appears to be completely embedded in the envelope of IC 1459. We detected an "S-shaped" disk in IC 1459 with a thick arc-like tail of about 3 arcmin protruding from the west side (see Fig. 2) and with $\mu_g \sim 26.5\,\mathrm{mag\,arcsec^{-2}}$.

A detailed inspection of the whole VST mosaic does not show any other low-surface-brightness features (at the imaging depth of the observations) in the intra-group space. The colour composite images given in Appendix B for the other group members show that all galaxies, except the faintest S0 IC 5269, have asymmetric outskirts. In particular, the spiral galaxy ESO 406-27 shows a prominent plume emerging from the disk to the NE, to which is associated an over-density of the HI gas (see Fig. B.5). All group members are described in Appendix A.

## 4.2. Isophotal analysis

In order to map the light and colour distribution for all group members, we performed the isophotal analysis using the IRAF task ELLIPSE (the position angle and the ellipticity are free parameters) on the final stacked image in each band out to the limiting radius estimated for each object (see Sect. 3). The method is the same as that adopted in previous studies based on the VEGAS data (Capaccioli et al. 2015; Iodice et al. 2016, 2017a, 2019; Spavone et al. 2017b, 2018; Cattapan et al. 2019). The isophote fit was performed for each galaxy by masking all the bright sources in the field (stars and background galaxies). In the case of IC 5264 and IC 5269B, which are close and/or embedded in the diffuse stellar envelope of IC 1459 (see Fig. 2), the isophote fit was performed after subtracting the two-dimensional model[5] of IC 1459.

From the isophotal analysis, we derived the azimuthally averaged surface-brightness, ellipticity ($\epsilon$), and position angle (PA) radial profiles in the $g$ and $r$ bands, the averaged extinction-corrected colour profiles, and the averaged $g - r$, $r - i$, and $g - i$ colour values. In addition, from the growth curve we estimated the total magnitude and effective radius in each band. Finally, using stellar population synthesis models (Ricciardelli et al. 2012; Vazdekis et al. 2012) with $\log Z/Z_\odot = 0$ and a Kroupa initial mass function and considering the average colour, we estimated the total stellar mass using the M/L ratio in the $g$ band (Iodice et al. 2017a; Spavone et al. 2018; Cattapan et al. 2019). Results are reported in Tables 3 and 4. For the BGG, IC 1459, the azimuthally averaged surface-brightness, ellipticity, and position angle radial profiles are shown in Fig. 3. Figure 4 shows the azimuthally averaged extinction-corrected colour profile and the two-dimensional $g - r$ colour map centred on IC 1459. The surface brightness profiles are PSF-deconvolved (see Capaccioli et al. 2015; Spavone et al. 2017b). For the other group galaxies the colour-composite image, the azimuthally averaged surface-brightness radial profiles in $g$, $r$, and $i$ band, and the azimuthally averaged extinction-corrected colour profiles are shown in Appendix B.

## 4.3. Fitting of the light distribution

In order to identify the main components dominating the galaxy light in IC 1459, we fitted the deconvolved surface-brightness radial profiles in the $g$ band. Since our aim is to compare the results of this fit with previously published ones, for consistency we use the $g$ band profile, as done for NGC 5018 (Spavone et al. 2018) and NGC 1533 (Cattapan et al. 2019).

The main outcome of the fitting is to map the stellar distribution in the outer envelopes of our sample galaxies. To this aim, according to Spavone et al. (2017b), we do not use the $\chi^2$ statistics in our fitting procedure. The data points corresponding to

---

[4] In this image we modelled and subtracted only the brightest regions of the close foreground stars. This prevents the subtraction of any physical faint feature overlapping the halo of the stars.

[5] The two-dimensional model of IC 1459 is based on the isophote fit and was derived using the task BMODEL in IRAF.
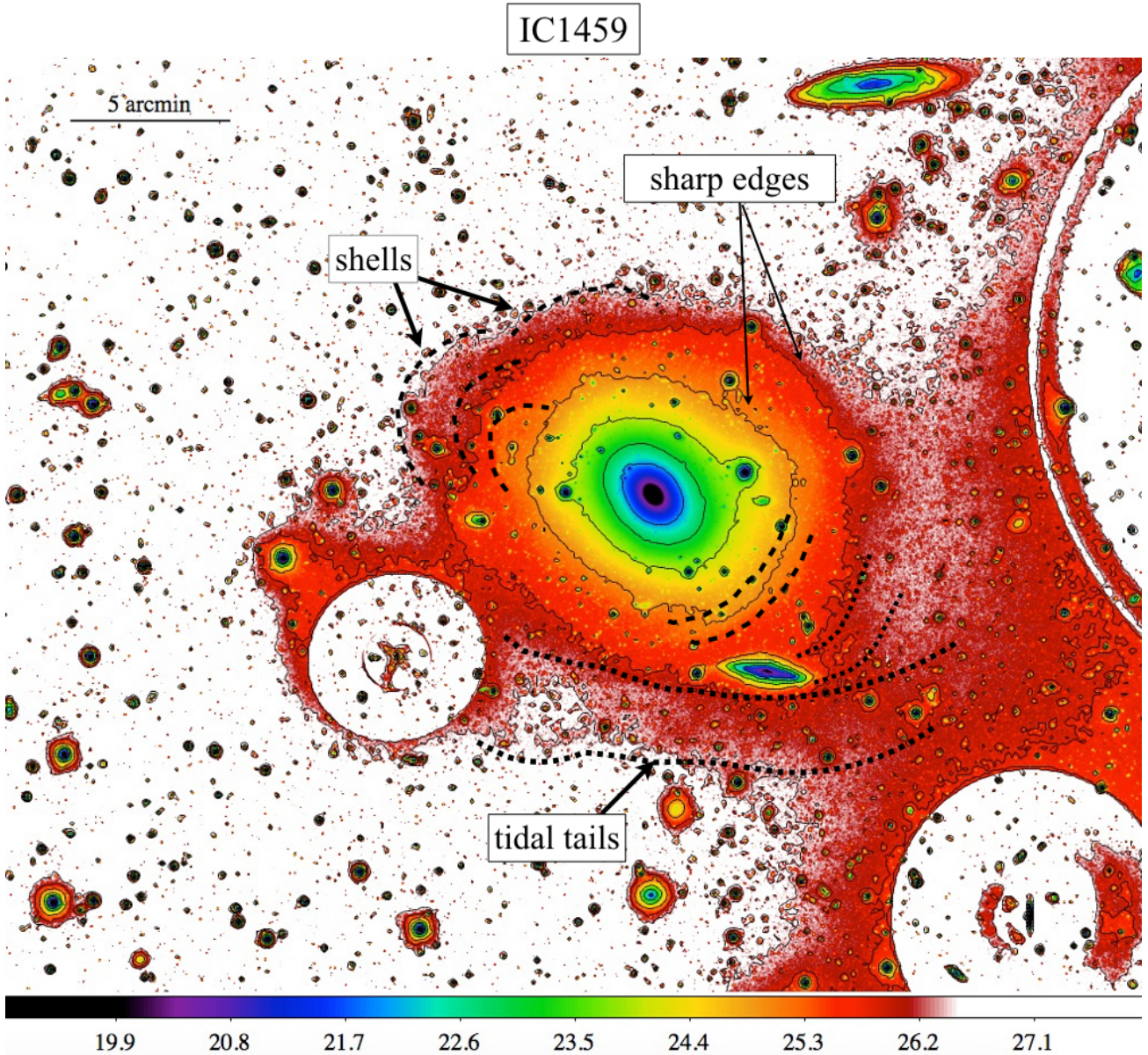
**Fig. 2.** Enlarged region ($\sim$52′ × 43′) of the VST mosaic around IC 1459 in the $g$ band. The image is in surface brightness levels given in the horizontal colour-bar. The solid contours correspond to the surface brightness levels: 22, 23, 24, 25, 26.4 mag arcsec$^{-2}$. The main low-surface-brightness features detected in the galaxy outskirts are marked on the image: dotted lines and dashed lines delimit the tidal tails and shells, respectively. The prominent sharp edges on the west side are also indicated with arrows (see text for details).

the central regions of the galaxies, with their small uncertainties, have considerable weight in determining the best-fit solution obtained by minimising the $\chi^2$, while the outer regions with greater errors have no weight. To avoid this problem, we adopted the same approach described by Seigar et al. (2007) and Spavone et al. (2017b): we performed least-square fits using a Levenberg–Marquardt algorithm, in which the function to be minimised is the rms scatter, defined as $\Delta = \sqrt{\frac{\sum_{i=1}^{m} \delta_i^2}{m}}$, where $m$ is the number of data points and $\delta_i$ is the $i$th residual. In order to account for the fainter stellar envelope in the most luminous ETGs, there is remarkable evidence from the recent deep surveys that the light profiles of these galaxies are not well fitted by a single Sérsic law and at least one additional component is needed to map the outer envelope contribution in the light distribution of the galaxy (see e.g. Seigar et al. 2007;

Donzelli et al. 2011; Arnaboldi et al. 2012; Huang et al. 2013; Iodice et al. 2016; Spavone et al. 2017a, 2018).

For this reason we fitted the azimuthally averaged surface-brightness radial profiles of IC 1459 combining a Sérsic law and an exponential function. From the total magnitude of the Sérsic and exponential component, $m_{\mathrm{tot,1}}$ and $m_{\mathrm{tot,2}}$ respectively, and taking into account the stellar mass-to-light ratio derived from the average $g - r$ colours (see Table 4), we derived the relative contribution of the outer envelope with respect to the total stellar mass of the galaxy ($f_{\mathrm{h}}$ in Table 5), which is about 37%. Results are listed in Table 5 and shown in Fig. 5.

Numerical simulations by Cooper et al. (2013) and Pillepich et al. (2018) suggest that the surface brightness profile of BCGs could be described by the superimposition of three components. In these simulations, the first Sérsic law represents the central in-situ component, and the second Sérsic

**Table 3.** Total magnitude and effective radius for the galaxies of the IC 1459 group.

| Galaxy | $m_g$ (mag) | $R_{e,g}$ (arcsec) | $m_r$ (mag) | $R_{e,r}$ (arcsec) | $m_i$ (mag) | $R_{e,i}$ (arcsec) |
|---|---|---|---|---|---|---|
| (1) | (2) | (3) | (4) | (5) | (6) | (7) |
| IC 1459 | 9.28 ± 0.07 | 177.00 ± 0.01 | 8.71 ± 0.07 | 133.60 ± 0.81 | 8.49 ± 0.01 | 50.8 ± 0.19 |
| IC 5269 | 12.58 ± 0.02 | 20.91 ± 0.20 | 12.01 ± 0.02 | 18.59 ± 0.33 | 11.24 ± 0.01 | 18.59 ± 0.33 |
| IC 5269B | 12.69 ± 0.02 | 67.42 ± 0.81 | 12.27 ± 0.02 | 68.49 ± 0.89 | 11.38 ± 0.03 | 88.31 ± 1.23 |
| IC 5270 | 12.24 ± 0.03 | 47.15 ± 1.81 | 11.72 ± 0.03 | 49.06 ± 0.89 | 11.04 ± 0.05 | 44.16 ± 0.79 |
| IC 5264 | 12.67 ± 0.03 | 30.21 ± 0.44 | 11.89 ± 0.04 | 34.34 ± 0.76 | 11.16 ± 0.04 | 31.55 ± 0.75 |
| ESO 406−27 | 12.86 ± 0.06 | 82.58 ± 3.18 | 12.73 ± 0.09 | 75.08 ± 5.95 | 12.38 ± 0.07 | 49.08 ± 1.09 |
| NGC 7418 | 10.31 ± 0.03 | 161.00 ± 2.49 | 10.01 ± 0.03 | 143.90 ± 2.36 | 9.94 ± 0.01 | 57.48 ± 0.37 |
| NGC 7421 | 11.93 ± 0.01 | 39.87 ± 1.83 | 11.53 ± 0.01 | 32.27 ± 0.07 | 10.81 ± 0.01 | 31.49 ± 0.16 |
| IC 5273 | 10.70 ± 0.04 | 99.77 ± 2.01 | 10.52 ± 0.03 | 77.70 ± 1.30 | 10.23 ± 0.02 | 41.11 ± 0.38 |

**Notes.** Column 1: galaxy name. Columns 2 and 3: total magnitude and effective radius in $g$ band. Columns 4 and 5: total magnitude and effective radius in $r$ band. Columns 6 and 7: total magnitude and effective radius in $i$ band.

**Table 4.** Colours and total stellar mass for the galaxies of the IC 1459 group.

| Galaxy | $A_{g'}$ (mag) | $A_{r'}$ (mag) | $A_{i'}$ (mag) | $g - r$ (mag) | $r - i$ (mag) | $g - i$ (mag) | $(\mathcal{M}/L)_g$ $(M_\odot/L_\odot)$ | $L_{tot,g}$ $(\times 10^{10} L_\odot)$ | $\mathcal{M}^*_{tot}$ $(\times 10^{10} M_\odot)$ |
|---|---|---|---|---|---|---|---|---|---|
| (1) | (2) | (3) | (4) | (5) | (6) | (7) | (8) | (9) | (10) |
| IC 1459 | 0.060 | 0.044 | 0.033 | 0.84 ± 0.31 | 0.51 ± 0.20 | 1.36 ± 0.30 | 5.695 | 17.70 | 100.80 |
| IC 5269B | 0.060 | 0.044 | 0.033 | 0.49 ± 0.10 | 0.65 ± 0.09 | 1.14 ± 0.18 | 0.656 | 0.77 | 0.50 |
| IC 5269 | 0.062 | 0.045 | 0.034 | 0.77 ± 0.25 | 0.71 ± 0.06 | 1.47 ± 0.19 | 3.921 | 0.85 | 3.32 |
| IC 5270 | 0.052 | 0.038 | 0.029 | 0.72 ± 0.09 | 0.65 ± 0.12 | 1.38 ± 0.15 | 2.335 | 1.16 | 2.71 |
| IC 5264 | 0.077 | 0.056 | 0.042 | 0.79 ± 0.06 | 0.81 ± 0.02 | 1.60 ± 0.05 | 4.301 | 0.78 | 3.35 |
| ESO 406−27 | 0.081 | 0.059 | 0.044 | 0.34 ± 0.20 | 0.45 ± 0.16 | 0.79 ± 0.16 | 0.488 | 0.65 | 0.32 |
| NGC 7418 | 0.060 | 0.044 | 0.033 | 0.66 ± 0.29 | 0.44 ± 0.57 | 1.09 ± 0.74 | 1.585 | 6.86 | 10.87 |
| NGC 7421 | 0.056 | 0.041 | 0.031 | 0.66 ± 0.24 | 0.68 ± 0.06 | 1.35 ± 0.23 | 1.585 | 1.54 | 2.44 |
| IC 5273 | 0.047 | 0.034 | 0.026 | 0.54 ± 0.15 | 0.51 ± 0.28 | 1.05 ± 0.40 | 0.701 | 4.78 | 3.36 |

**Notes.** Column 1: galaxy name. Columns 2–4: extinction correction in the $g$, $r$, and $i$ band from NED. Columns 5–7: averaged extinction-corrected $g - r$, $r - i$, and $g - i$ colour value. Column 8: mass-to-light ration in $g$ band. Column 9: total stellar luminosity in $g$ band. Column 10: total stellar mass.
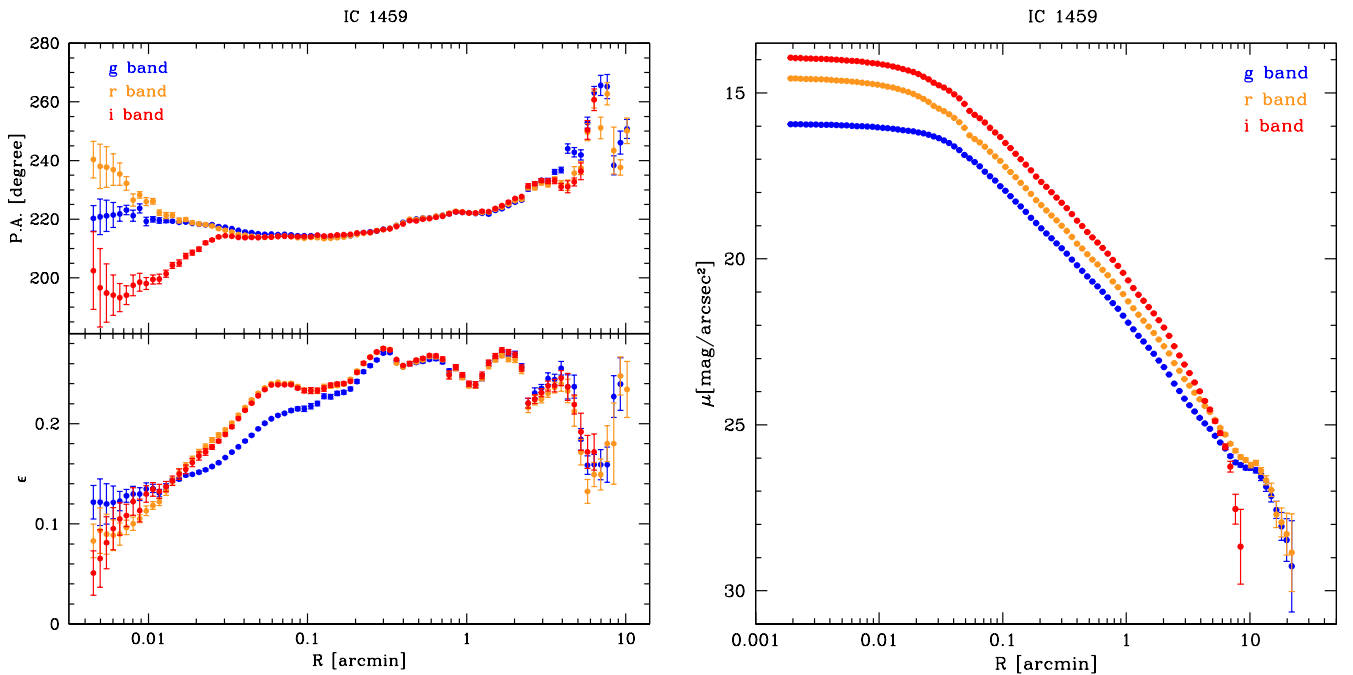


**Fig. 3.** Results from the isophotal analysis for IC 1459. Ellipticity and position angle radial profiles are shown in the *left lower* and *upper panel*, respectively. The azimuthally averaged and PSF-deconvolved surface-brightness radial profile of IC 1459 is plotted in the *right panel*.
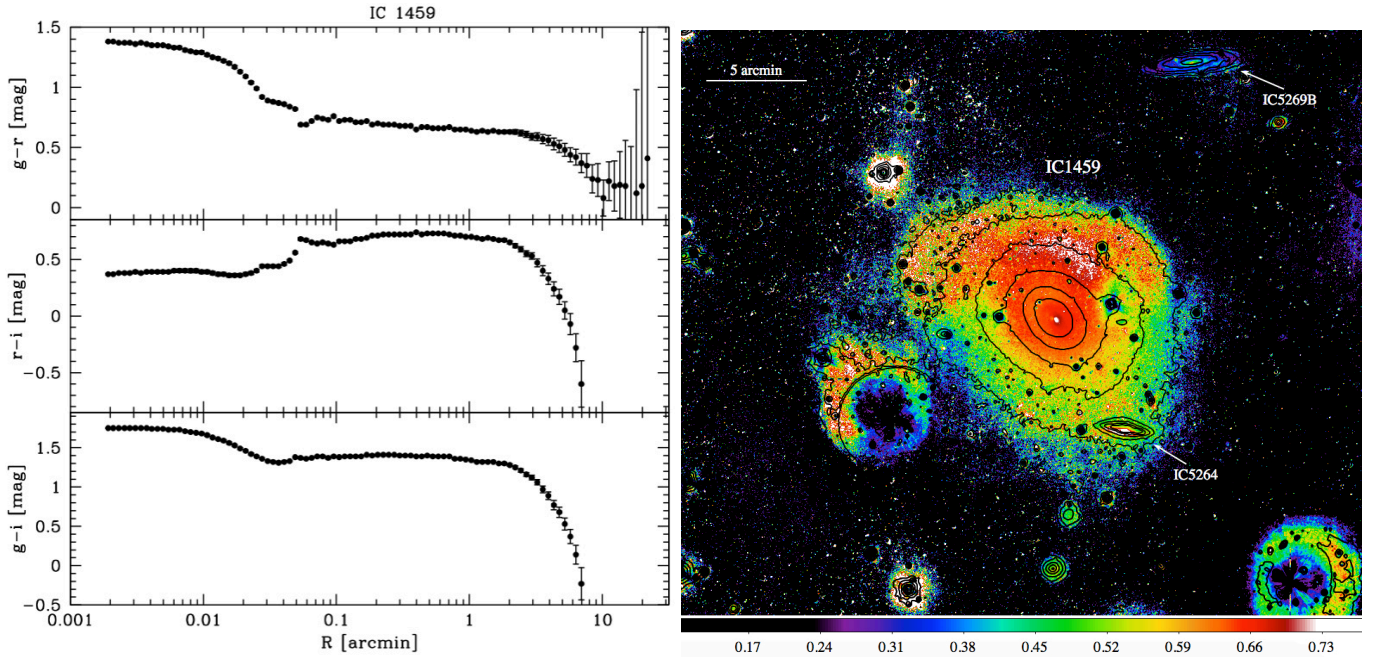
**Fig. 4.** *Left panel*: azimuthally averaged, PSF-deconvolved, and extinction-corrected colour radial profiles of IC 1459. *Right panel*: two-dimensional colour map centred on IC 1459, the image size is $35.42'.7 \times 29.05'.7$ with north at the top and east to the left. The horizontal colour bar gives the $g-r$ colour scale. The solid contours correspond to the following surface brightness levels in the $g$ band: 22, 23, 24, 25, 26.4 mag arcsec$^{-2}$.

law and third exponential function represent the accreted components, the relaxed and unrelaxed, respectively. As discussed in detail by Spavone et al. (2017a,b), in order to compare observations and theoretical predictions, we used numerical simulations as a "guide" for the decomposition, and also fitted the light distribution of IC 1459 with a three-component model, where the inner Sérsic component was meant to mimic the in-situ component predicted by the above numerical simulations. The fitted parameters are listed in Table 5. Figure 5 shows the results of the three-component fits. Looking at the rms scatter $\Delta$ of the fits, we can clearly see that by adding the third component we achieve an improvement of at least 4%. Since the expected value of $\Delta$ scales as $\sqrt{(m-k)/m}$ (see Seigar et al. 2007), where $m$ is the number of measured points ($\sim$70 in our case) and $k$ is the number of free parameters, we would need 11 free parameters to obtain an improvement of 4%. This means that the improvement we obtain in our fit is not only due to the introduction of additional free parameters, as already shown by Seigar et al. (2007) and Spavone et al. (2017b).

From the three-component model, we estimated the transition radius $R_{\rm tr} = 3'.1 \simeq 25.7$ kpc, which is the distance from the galaxy centre at which the unrelaxed component starts to dominate the light distribution of the BGG (Cooper et al. 2013). From the two accreted stellar components, the relaxed and unrelaxed ones described by the second Sérsic law and exponential function, we estimate a total accreted mass fraction of 87% in IC 1459, which corresponds to $8.77 \times 10^{11} \, M_\odot$ (see Table 6). This is the relative contribution of the accreted components with respect to the total stellar mass of the galaxy, $f_{\rm h,T}$, to be compared with the predictions for this quantity by the numerical simulations cited above. The comparison is given in Fig. 7 and discussed in Sect. 6.1. The error bars on the datapoint have been derived by means of error propagation on $M_\star$ and $M_{\rm acc}$, which are 0.02 and 0.04, respectively. Table 6 reports the values of transition radius, mass-to-light ratio, total stellar mass, and accreted mass fraction of IC 1459.

### 4.4. Intragroup light

As stated before, after detailed inspection of the deep VST mosaic we do not detect any intragroup low-surface-brightness features in the form of stellar tails or streams between and/or around the group members, except for those in the outskirts of IC 1459 (see Sect. 4.1 and Fig. 2). Therefore, we consider this area to be the bulk of the IGL and focused on it to estimate the total flux in this component. To this aim, we modelled the light distribution in the $g$ band of the dominant member IC 1459 with the IRAF task BMODEL. This task creates a two-dimensional noiseless photometric model of the galaxy from the result of the isophotal analysis generated by ELLIPSE by taking into account the variations in the ellipticity and position angle. We derived the residual image by subtracting the two-dimensional model from the parent image. All the foreground and background sources in the residual image were masked. In particular, for the three brightest stars in the area, namely HD 216666 ($\alpha_{\rm J2000} = 22^{\rm h}55^{\rm m}14^{\rm s}.947$ and $\delta_{\rm J2000} = -36°23'19''.18$), HD 216781 ($\alpha_{\rm J2000} = 22^{\rm h}56^{\rm m}12^{\rm s}.13$ and $\delta_{\rm J2000} = -36°40'49''.3$), and HD 216972 ($\alpha_{\rm J2000} = 22^{\rm h}57^{\rm m}50^{\rm s}.33$ and $\delta_{\rm J2000} = -36°32'45''.8$)[6], masks extend out to regions where scattered light is detected (see Fig. 2). The IGL region is defined with the IRAF task POLYMARK and is about 23 arcmin$^2$ around IC 1459. From the fit of the light profiles, we know that the stellar envelope starts to dominate at $R \geq R_{\rm tr} = 3'.1 = 25.77$ kpc (see Sect. 4.3). Therefore, for the IGL estimate we account for the flux from $R \geq R_{\rm tr}$, and the inner regions of the galaxy (at smaller radii) are masked.

From the defined regions, we derived the integrated extinction-corrected magnitude of the IGL. The total luminosity of the IGL in $g$ band is $5.25 \times 10^9 \, L_\odot$, which accounts for 2% of the total light of the group and 3% of the light of IC 1459 (see Table 7). The error estimate on the flux in the selected area takes

---

[6] The stars coordinates are from HYPERLEDA.

**Table 5.** Best-fitting structural parameters for the multi-component fit of the surface-brightness radial profile of IC 1459 in $g$ band.

| Models | $R_{e,1}$ | | $n_1$ | $\mu_{e,1}$ | $R_{e,2}$ | | $n_2$ | $\mu_{e,2}$ | $r_h$ | | $\mu_0$ | $f_{h,T}$ |
|---|---|---|---|---|---|---|---|---|---|---|---|---|
| | (arcsec) | (kpc) | | (mag arcsec$^{-2}$) | (arcsec) | (kpc) | | (mag arcsec$^{-2}$) | (arcsec) | (kpc) | (mag arcsec$^{-2}$) | |
| (1) | (2) | | (3) | (4) | (5) | | (6) | (7) | (8) | | (9) | (10) |
| 2 | $53.79 \pm 0.06$ | 7.15 | $5.3 \pm 0.7$ | $21.7 \pm 0.5$ | . . . | . . . | . . . | . . . | $390 \pm 1$ | 52.61 | $25.18 \pm 0.01$ | 37% |
| 3 | $5.54 \pm 0.12$ | 0.67 | $1.61 \pm 0.06$ | $18.19 \pm 0.04$ | $54 \pm 1$ | 7.28 | $2.12 \pm 0.12$ | $21.69 \pm 0.05$ | $329 \pm 4$ | 44.38 | $24.49 \pm 0.11$ | 87% |

**Notes.** Best-fit parameters of the PSF-deconvolved light profile decomposition: Col. 1: number of functions of the multi-component fit applied. Columns 2–4: effective radius, Sérsic index, and effective surface brightness of the first Sérsic component. Columns 5–7: effective radius, Sérsic index, and effective surface brightness of the second Sérsic component. Columns 8 and 9: scale radius and central surface brightness of the exponential component. Column 10: accreted mass fraction.

## 5. A deep view of the IC 1459 group

Deep OmegaCAM at VST data allow us to map the azymuthally averaged surface brightness of IC 1459 down to $\mu_g = 29 \pm 1$ mag arcsec$^{-2}$ and $\mu_r = 29 \pm 1$ mag arcsec$^{-2}$ at $R = 21\farcs83 \simeq 181.1$ kpc (~7.4$R_e$ in $g$ and ~9.8$R_e$ in $r$ band; see right panel of Fig. 3). Images in the $i$ band are shallower (see Table 2 and Sect. 3), which causes the observed drop of the surface brightness profile in this band (see Fig. 3). IC 1459 is the biggest and the reddest galaxy of the group, with $R_{e,g} \simeq 23.9$ kpc and $g - r = 0.84$ mag (Table 3). By fitting the light distribution we found that the outer stellar envelope starts to dominates the light for $R \geq 5$ arcmin (see Sect. 4.3 and Table 5). The other group members are LTGs, except for IC 5269 which is classified as an S0 (see Fig. 1). The main properties of LTGs (i.e. total luminosity, effective radius, and average colours) are given in Tables 3 and 4.

The enlarged region of the VST mosaic around IC 1459 in the $g$-band surface brightness levels (see Fig. 2) highlights the structure of the IC 1459 outer envelope (i.e. at $R \geq 5$ arcmin). There are shells in the northeast and southwest regions and prominent sharp edges on the west side. We detected an elongated tidal tail to the south, and a thick arc-like tail protruding on the west side of the small group member IC 5264. The isophotal analysis shows that the outer envelope has a twist in the position angle profile of about 40 degrees and a scatter in the roundish ellipticity profile (see left panel of Fig. 3).

The inside 1 arcmin (~8 kpc) of the averaged colour profile for IC 1459 (Fig. 4, left panel) has redder colours, where $g - r$ varies in the range 0.5–1.5 mag. This is the region where Forbes et al. (1995, and references therein) detected an arcsec-scale dust lane crossing the galaxy nucleus. At larger radii, the colour profiles decline toward bluer colours, with $g - r \leq 0.5$ mag. The two-dimensional colour map (Fig. 4, right panel) shows an asymmetric distribution of the colour: in the north, there is an arc-like structure, extending from east to west, and characterised by very red colours ($g - r \geq 0.6$ mag). This structure corresponds to the region where shells are detected in the envelope. In the region of the tidal tail (in the south) the envelope has bluer colours ($g - r \simeq 0.6$ mag). The small peculiar LTG ESO 406−27 in the group, which is located in this region, is the bluest galaxy of the group ($g - r \sim 0.34$, Table 4). The existence of the blue tidal tails close to ESO 406−27 could be interpreted as evidence in support of the previous hypothesis that there is a possible ongoing interaction of this galaxy with IC 1459 (Serra et al. 2015; Saponara et al. 2018).

Figure 1 shows the VST $g$ band mosaic of the group with the HI map from Oosterloo et al. (2018). There is a lot of HI associated to LTGs, showing a different degree of asymmetry and off-centre distribution with respect to the stellar disk. In the region of the BGG there are signatures of HI stripping from gas-rich galaxies (Saponara et al. 2018), such as for example the northeast to southwest low-surface-brightness HI tail (Oosterloo et al. 2018). The possible HI donors of this debris are IC 5264 and ESO 406−27 (Saponara et al. 2018; Oosterloo et al. 2018). In the NE of IC 1459, the HI does not seem to be associated with galaxies: the deep VST images show that this is the region where shells in the envelope are detected. In the southern part of the IC 1459 envelope, the HI distribution is also elongated EW, overlapping the region where the faint tidal tail is found (see Fig. 2). Furthermore, more in the south, we found a faint diffuse light over-density north of ESO 406−27 (see Fig. B.5), which would be consistent with the interaction scenario proposed by Serra et al. (2015), Saponara et al. (2018), and Oosterloo et al. (2018) involving IC 5264 and ESO 406−27.

In conclusion, the faint features detected in the envelope of IC 1459 provide evidence of the ongoing accretion process on the BGG. Furthermore, the interaction and tidal effects could be responsible of HI stripped debris and of the faint optical counterparts found in two group members (Kilborn et al. 2009; Serra et al. 2015; Saponara et al. 2018).

## 6. IC 1459 versus other loose groups of galaxies

In this section we compare the main observed properties of the IC 1459 group with those available for the other two groups of galaxies centred on NGC 5018 (Spavone et al. 2018) and NGC 1533 (Cattapan et al. 2019). The comparison is motivated by consistency in the data set and in the total mass of the systems. All groups are targets of the VEGAS sample. Therefore, all data were obtained with the same telescope and with the same observing strategy and therefore have comparable depth and accuracy. Furthermore, for the data analysis (i.e. isophote fit, fitting of the surface brightness profiles, colour estimate) we adopted the same tools and procedures as described in Sect. 4. In addition, the three groups have the virial mass of the same order of magnitude. NGC 5018 and NGC 1533 groups have comparable virial radius and mass, with $R_{vir} = 0.4$ Mpc and $M_{vir} \sim 7 \times 10^{12} M_\odot$ for NGC 5018, and $R_{vir} = 0.4$ Mpc and $M_{vir} \sim 5 \times 10^{12} M_\odot$ for NGC 1533 (Gourgoulhon et al. 1992; Firth et al. 2006), whereas IC 1459 is a massive system, with $R_{vir} = 0.21$ Mpc and $M_{vir} \sim 3.710^{13} M_\odot$ (see Sect. 2 and Brough et al. 2006).

In the following sections, we compare the characteristics of the BGGs, the stellar halo properties, the amount of IGL, and the HI mass and distribution. This helps to trace the different
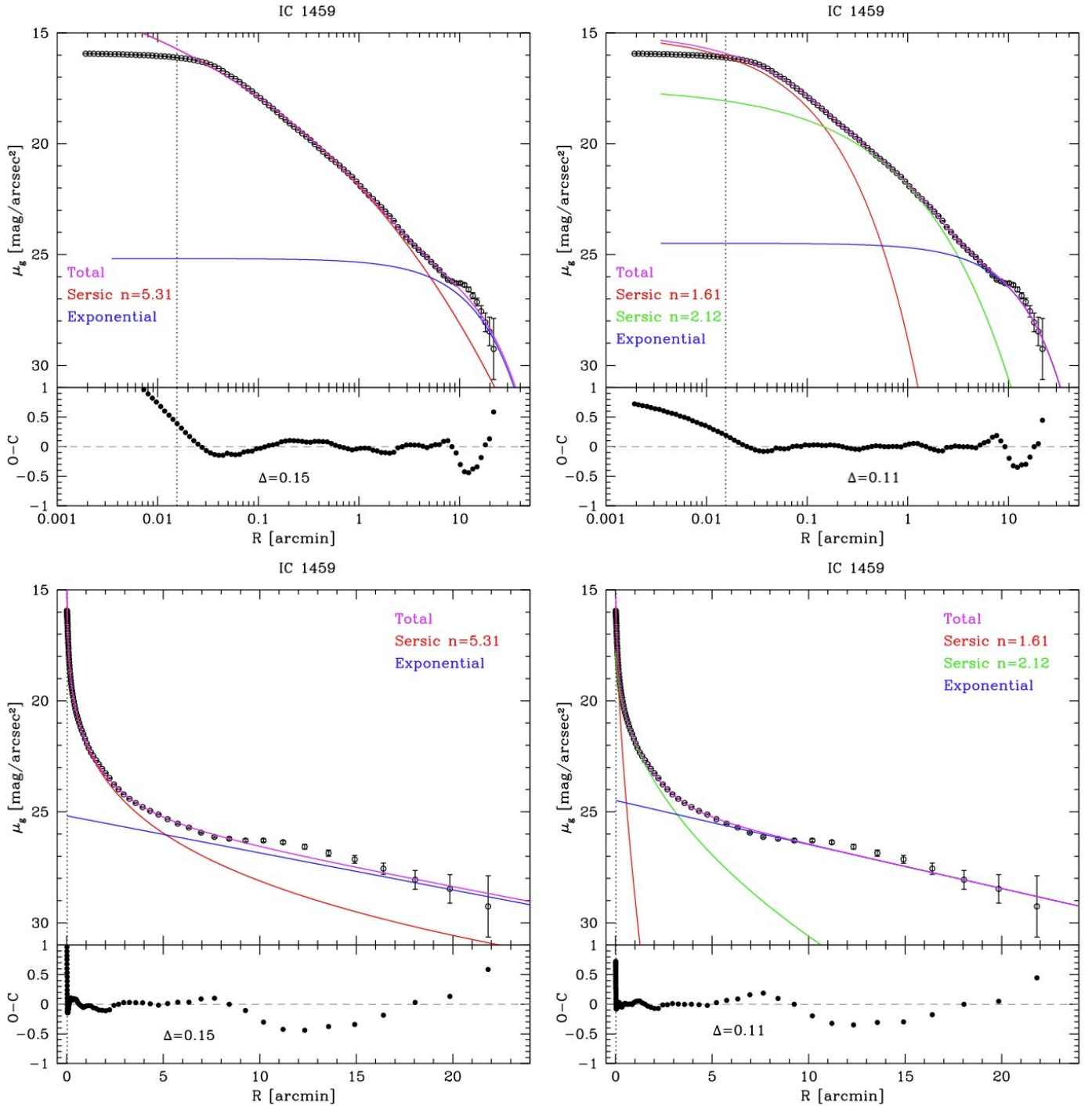
**Fig. 5.** Surface-brightness radial profile of IC 1459 in *g* band (black open circles) on a logarithmic (*top panels*) and linear scale (*bottom panels*) fitted with a two-component model (*left panels*) and with a three-component model (*right panels*). The red solid line is the first Sérsic component, the green solid line is the second Sérsic component, the blue solid line is the exponential component, and the magenta solid line marks the model of the total light distribution. The black vertical dotted line marks the core of the galaxy which was excluded in the fit ($R < 0\rlap.''9$). The $O - C$ panel (black filled circles) represents the residual between the azimuthally averaged surface-brightness radial profile and the multi-component model. $\Delta$ is the rms scatter minimised by the Levenberg–Marquardt algorithm (Seigar et al. 2007).

evolutionary stages and how this could reflect in the observed properties.

An overall and preliminary picture of the evolutionary stage of the groups is carried out here using the colour-magnitude diagram (CMD). Here it is possible to trace the galaxy transformation from active and star-forming (Blue Cloud, BC) to passively evolving (Red Sequence, RS) via the Green Valley (GV; see e.g.

Mazzei et al. 2014, and references therein). Figure 6 shows the CMD of the three analysed low-density environments. The BGG of the NGC 5018 group, NGC 5018, seems to be a typical red and dead ETG, and the other two galaxies (NGC 5022 and MCG-03-34-013) are in the GV approaching the RS. The very red NUV-r colours for NGC 5018 could arguably be due to the large amount of dust in the galaxy centre (Spavone et al. 2018), which affects

**Table 6.** Main properties of the BGG sample.

| BGG | $g-r$ (mag) | $(M/L)_g$ | $\mathcal{M}^*_{tot}$ $(\times 10^{11}\,M_\odot)$ | $f_{h,T}$ | $\mathcal{M}^*_{tot\,acc}$ $(\times 10^{11}\,M_\odot)$ | $R_e$ (kpc) | $R_{tr}/R_e$ | $\mu_{tr}$ (mag arcsec$^{-2}$) | $(g-r)_{R<R_{tr}}$ (mag) | $(g-r)_{R>R_{tr}}$ (mag) |
|---|---|---|---|---|---|---|---|---|---|---|
| (1) | (2) | (3) | (4) | (5) | (6) | (7) | (8) | (9) | (10) | (11) |
| NGC 5018 | $0.70 \pm 0.20$ | 1.97 | 2.9 | 92% | 2.7 | 6.37 | 5.37 | 26.6 | 0.78 | 0.94 |
| NGC 1533 | $0.77 \pm 0.05$ | 3.92 | 1.17 | 78% | 0.91 | 6.35 | 2.80 | 27.2 | $0.77 \pm 0.04$ | $0.49 \pm 0.29$ |
| IC 1459 | $0.84 \pm 0.31$ | 5.70 | 10.08 | 87% | 8.77 | 24.47 | 1.05 | 25.1 | $0.89 \pm 0.29$ | $0.44 \pm 0.11$ |

**Notes.** Column 1: BGG name. Column 2: averaged extinction-corrected $g-r$ colour value. Column 3: mass-to-light ratio in $g$ band. Column 4: total stellar mass. Columns 5 and 6: total accreted stellar mass fraction from the multi-component fit in $g$ band and value in solar masses. Column 7: effective radius in $g$ band. Columns 8 and 9: transition radius normalised to the effective radius and corresponding surface brightness. Columns 10 and 11: averaged extinction-corrected $g-r$ colour value inside and outside the transition radius.

**Table 7.** Properties of galaxy group sample.

| Group | N | ETGs/LTGs | $m_{IGL,g}$ (mag) | $L_{IGL,g}$ $(\times 10^9\,L_\odot)$ | $(L_{IGL}/L_{BGG})_g$ | $(L_{IGL}/L_{Group})_g$ | $\mathcal{M}_{HI}$ $(\times 10^9\,M_\odot)$ | $D$ (Mpc) |
|---|---|---|---|---|---|---|---|---|
| (1) | (2) | (3) | (4) | (5) | (6) | (7) | (8) | (9) |
| NGC 5018 | 3 | 1.6 | 11.39 | 70.60 | 47% | 41% | 2.4 | 31.4 |
| NGC 1533 | 3 | 1.6 | 14.17 | 3.46 | 12% | 8% | 7.7 | 21.0 |
| IC 1459 | 9 | 0.3 | 13.10 | 7.17 | 4% | 2% | 22.2 | 28.7 |

**Notes.** Column 1: group name. Columns 2 and 3: number of bright galaxies in the group ($M_g < -17$) and fraction of ETGs. Columns 4 and 5: integrated magnitude and luminosity in $g$ band of the IGL. Columns 6 and 7: fraction of intragroup light divided by the BGG luminosity and total luminosity of the group. Column 8: total HI mass associated to the group. Column 9: distance of the group used to estimate the total HI mass; for NGC 5018 by Kim et al. (1988), for NGC 1533 by Kilborn et al. (2005) and for IC 1459 by Kilborn et al. (2009).

the NUV flux. In the NGC 1533 triplet, the BGG (NGC 1533) is in the RS, while the other ETG (IC 2039) is very close to the RS, and the LTG (IC 2038) has just left the BC. The CMD of the entire backbone of the Dorado group, including the NGC 1533 triplet, has been shown by Cattapan et al. (2019). The Dorado backbone has an extended and rich RS. IC 1459 and IC 5269 are the two ETGs of the IC 1459 group and they lie in the RS, as expected. IC 5264 is the LTG that lies in projection of the stellar halo of IC 1459 and is in the GV. All the other LTGs, except for ESO 406−27 which is in the BC, are leaving the BC to migrate to the GV.

This means that the IC 1459 group is a typical young galaxy group with a significant BC and a depopulated RS. The NGC 5018 group on the other hand represents what happens for more evolved galaxy systems which have a well-defined RS and a poor or empty BC (Cattapan et al. 2019, and references therein).

### 6.1. The accreted mass fraction of BGGs

The three BGGs we analyse are NGC 5018, NGC 1533, and IC 1459. Of these, IC 1459 is the brightest ($L^*_{tot} = 1.77 \times 10^{11}\,L_\odot$), most massive ($\mathcal{M}^*_{tot} = 10.08 \times 10^{11}\,M_\odot$), and reddest galaxy ($g - r = 0.84$ mag), while NGC 1533 is the least luminous ($L^*_{tot} = 2.99 \times 10^{10}\,L_\odot$) and least massive ($\mathcal{M}^*_{tot} = 2.9 \times 10^{11}\,M_\odot$). Finally, NGC 5018 is the bluest galaxy ($g - r = 0.7$ mag). The properties of the BGGs are listed in Table 6. In Fig. 7 we show the accreted mass fraction as a function of the total stellar mass for the analysed BGGs/BCGs in VEGAS (Iodice et al. 2016, 2017b; Spavone et al. 2017b, 2018; Cattapan et al. 2019) and for the other BGGs/BCGs in the literature (Seigar et al. 2007; Bender et al. 2015). We compare these results with the theoretical predictions of cosmological galaxy formation by Cooper et al. (2013, 2015) and with the Illustris simulations by

Pillepich et al. (2018, their Fig. 12). We find that the accreted mass fraction for the three BGGs (IC 1459, NGC 5018, and NGC 1533) is in the range of 78–92% (Table 6). These values are comparable with those obtained for other BCGs and BGGs in the VEGAS sample, as well as with literature data (see Fig. 7). Moreover, the accreted mass fraction estimated for IC 1459 and previously for NGC 5018 and NGC 1533 is consistent with the theoretical predictions, which suggest that stars accreted by BCGs and BGGs in the stellar mass range $10^{11}-10^{13}$ account for most of their total stellar mass (Cooper et al. 2013; Pillepich et al. 2018).

The above result also suggests that the accreted stellar mass fraction seems to be a function of the total stellar mass rather than of the environment, since the BGGs have comparable accreted mass to the bright cluster members (Fig. 7). This lack of correlation between accreted mass fraction and environment is a very recent studied topic and has been investigated further for BCGs by DeMaio et al. (2018).

### 6.2. The stellar envelope of the BGGs

By fitting the light distribution, we were able to set the scales of the different components in the galaxy structure. In particular, we estimated the transition radius where the outer stellar and faint envelope starts to dominate the light (see Sect. 4.3). The stellar envelopes of the three BGGs studied in this work occur at surface brightness levels $25.1 < \mu_g < 27.2$ mag arcsec$^{-2}$ (see Table 6), which is comparable with the surface brightness of the stellar envelopes observed in other BCGs (Spavone et al. 2017a, $24.0 < \mu_g < 27.8$ mag arcsec$^{-2}$) and even consistent with the theoretical predictions. In the three BGGs, the transition in the surface brightness profiles also corresponds to a transition in the ellipticity, position angle, and colour profiles. In particular, the outer isophotes are more elongated or rounder than the
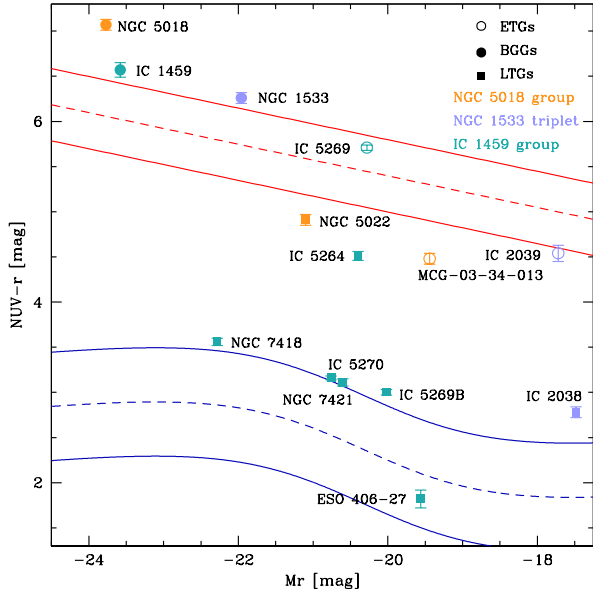
**Fig. 6.** $M_r$ vs. $(NUV - r)$ colour-magnitude diagram of the three loose groups: the NGC 5018 group (orange points), the NGC 1533 triplet (mauve points), and the IC 1459 group (teal points). The Wyder et al. (2007) fits (dashed lines) and the error estimations (solid lines) for the Red Sequence (red lines) and Blue Cloud (blue lines) are shown. Open circles mark early-type galaxies (ETGs), filled circles mark the BGGs, and filled squares mark LTGs. The NUV data are from NED, while the $r$ band data for the NGC 5018 group are from Spavone et al. (2018), the data for the NGC 1533 triplet are from Cattapan et al. (2019), and the data for the IC 1459 group are presented in this work.

inner ones and are twisted (see Fig. 3 and Spavone et al. 2017a, 2018; Cattapan et al. 2019).

Figure 8 compares the azimuthally averaged surface brightness (in the $g$ band) and colour profiles for the three BGGs, scaled to their effective magnitude, as a function of $R/R_e$. This reveals that NGC 5018 has the most extended envelope, out to $30R_e$, which is also quite red $(g - r)_{R>R_{tr}} = 0.94$ mag. IC 1459 and NGC 1533 have smaller ($\sim 10R_e$) and bluer envelopes, with $(g - r)_{R>R_{tr}} = 0.44$ mag and $(g - r)_{R>R_{tr}} = 0.49$ mag, respectively. At radii larger than $R_{tr}$ (i.e. $\geq 2R_e$), the surface brightness profiles show that the contribution from the stellar envelope in NGC 5018 and IC 1459 to the total light is larger than that in NGC 1533. This is consistent with a higher accreted mass fraction estimated in the former two galaxies (see Table 6).

According to theoretical predictions on the mass assembly for the BCGs and BGGs, the morphology of the outskirts, the shape of the light profiles, and the colour distribution reflect the different accretion processes and progenitors (Cooper et al. 2010; D'Souza et al. 2014; Monachesi et al. 2019; Mancillas et al. 2019). The gradual accretion of small-mass satellites produces streams, while intermediate and major merging generates shells and tidal tails. In the outskirts of three BGGs, the deep VEGAS images have shown such features, suggesting that the mass assembly is still ongoing. The most prominent and luminous tidal tails are observed in the NGC 5018 group, in the intra-group space, and protruding from the BGG (Spavone et al. 2018). In IC 1459 (this work) and in NGC 1533 we observe very faint tidal tails, which are probably tracing the interaction with the smaller group members close to the BGG, and several shells in the outskirts (Cattapan et al. 2019).

According to Mancillas et al. (2019), the evolution of the number of tidal tails does not change with the age of the BCG and BGG; the expected number is from one to three at most
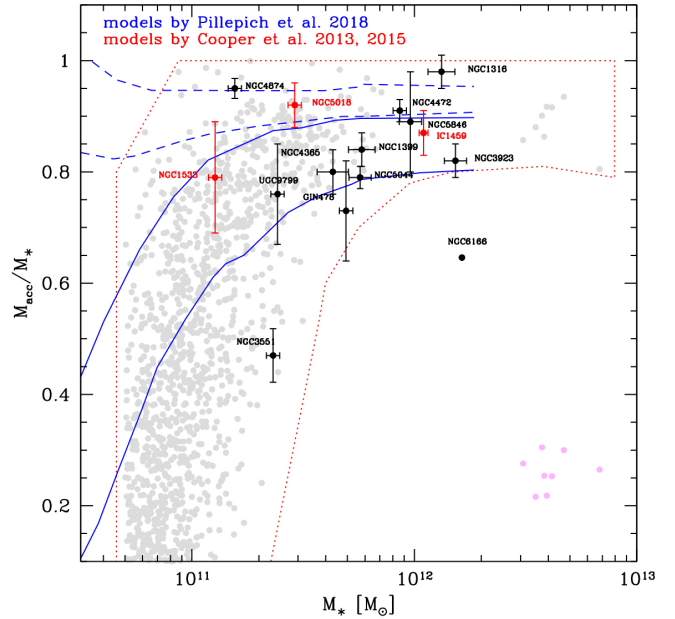
**Fig. 7.** Accreted mass fraction as a function of total stellar mass for ETGs. The measurements for NGC 5018, NGC 1533, and IC 1459 (from the three-components fit) are given as red circles. Black circles correspond to other BGGs/BCGs from the literature (Seigar et al. 2007; Bender et al. 2015; Iodice et al. 2016, 2017b; Spavone et al. 2017b, 2018). The region within the red dashed lines and the grey filled circles corresponds to the predictions of cosmological galaxy formation simulations by Cooper et al. (2013, 2015). The regions brackets by the blue continuous and dashed lines indicate the accreted mass fraction measured in the Illustris simulations by Pillepich et al. (2018, see their Fig. 12) within 30 kpc and outside 100 kpc, respectively. Magenta filled circles show the mass fraction associated with the streams from Table 1 in Cooper et al. (2015).

and these have a short survival time of $\sim 2$ Gyr. Stellar streams show a peak in number (reaching 8 to 10) around 10 Gyr of the galaxy age, and decreasing in number for older galaxies, since they tend to be dissolved in the halo. Shells strongly depend on the inclination, and therefore the prediction on the detectable number changes from four to eight for a galaxy with an age of 10 Gyr. Both streams and shells are longer-lived than tidal tails, surviving until 4 Gyr. Taking this into account, as well as the fact that the last burst of star formation for NGC 5018 is about 4 Gyr (Spavone et al. 2018) whereas in IC 1459 and NGC 1533 it is older (around 10 Gyr), the expected number of tidal tails is consistent with the observations in the same range of surface brightness levels. The number of shells and streams observed in IC 1459 and NGC 1533 is also consistent with simulations in the range of ages estimated for these two galaxies. The absence or low number of faint streams and shells in NGC 5018 is also expected from simulations for galaxies of comparable age.

In summary, the difference or similarity in the global properties (light profiles and substructures) of the stellar envelope in three BGGs could be used to constrain the phase and/or the mechanism in the mass assembly. In particular, NGC 5018 might have experienced strong tidal forces in the last 2 Gyr during the interaction with its bright companion galaxy, which lead to the prominent tidal tail. Alternatively, as the IC 1459 and NGC 1533 groups are populated by less luminous galaxies close to the BGG, this suggests that their stellar halo is assembling by minor and intermediate merging, which shaped the observed shells and streams.
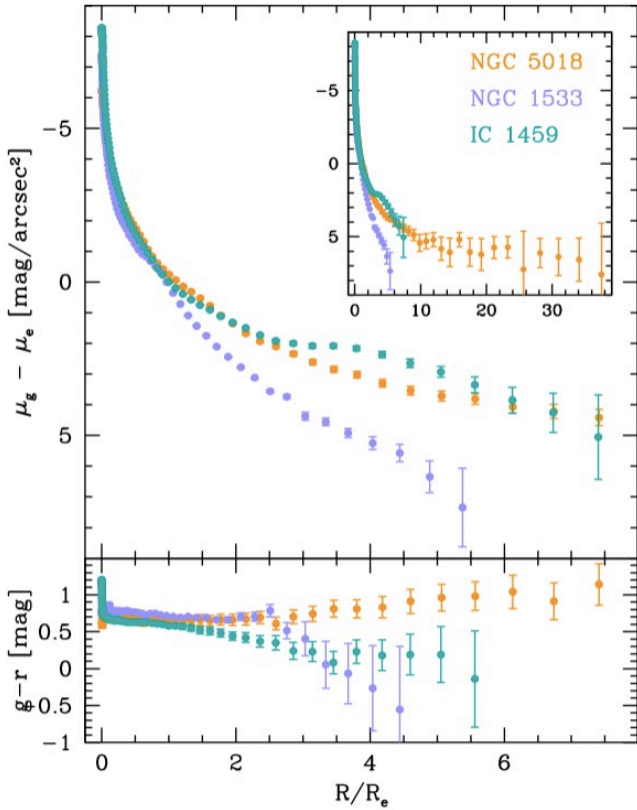
**Fig. 8.** Azimuthally averaged surface-brightness (*top panel*) and colour normalised (*bottom panel*) radial profiles of NGC 5018 (orange), NGC 1533 (mauve), and IC 1459 (teal) in *g* band scaled to their effective surface brightness, $\mu_e$, as a function of the semi-major axis normalised to the effective radius, $R/R_e$.

### 6.3. Intragroup light

In Fig. 9 (top panel) we compare the fraction of IGL, with respect to the total light in the group, as a function of the virial mass available for several groups of galaxies, including the estimates we derived for three systems discussed in this work. Although the sample is composed of eight groups in total, the large scatter suggests that there is no clear trend of IGL with virial mass. For massive clusters of galaxies ($M_{vir} \geq 10^{13}$), this result would be consistent with theoretical predictions from Contini et al. (2014) and Rudick et al. (2011) where the relations between ICL and virial mass are relatively flat. On the other hand, the different IGL values found in the three groups is consistent with previous observations indicating that the higher the ETG/LTG ratio, the greater the IGL component (Da Rocha et al. 2008). As pointed out by Da Rocha et al. (2008), the low IGL fraction is expected for groups that are dominated by LTGs and still have HI in the discs of the galaxies. The NGC 5018 group and the NGC 1533 triplet are composed of two ETGs and one LTG (Spavone et al. 2018; Cattapan et al. 2019), while the IC 1459 group counts only two ETGs, IC 1459 and IC 5269, that is the ETG/LTG ratio is relatively low: ETG/LTG = 0.29 (Table 7). The IGL component of the NGC 5018 group is the highest (~41%) between the three groups studied here. A smaller fraction of IGL is derived for the other two systems, namely ~8% for the NGC 1533 triplet and ~2% for the IC 1459 group (Table 7). Compared to the other two groups, IC 1459 has a large amount of HI associated to the LTG group members. All others groups of galaxies included in Fig. 9 are Hickson compact groups (HCGs), which are usually characterised by a high ETG/LTG ratio (Hickson et al. 1992).
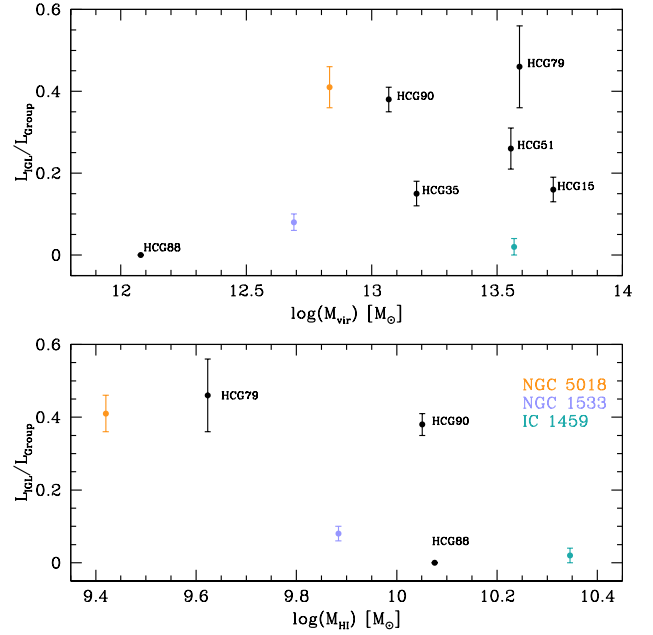


**Fig. 9.** Luminosity of the IGL component normalised to the total group luminosity as a function of the total HI mass of the group (*lower panel*) and of the virial mass of the group (*top panel*), for NGC 5018 group (orange), NGC 1533 triplet (mauve), and IC 1459 group (teal). Values are compared with those for several HCGs. For HCG 79 and HCG 88 data are from Borthakur et al. (2010), Da Rocha & Mendes de Oliveira (2005), Ribeiro et al. (1998) and Nishiura et al. (2000). For the remaining HCGs, data are taken from Da Rocha et al. (2008) and Selim & Iqbal (2008).

The IGL fraction obtained for NGC 5018 (Spavone et al. 2018) is similar to the IGL estimated for HCG 90 (White et al. 2003), which is a strongly interacting system with $L_{IGL}/L_{Group} \sim 38\%$ of comparable virial mass. The HCG 88 is the only system of the HCG sample that shows no IGL component, down to the surface brightness detection limit (Da Rocha et al. 2008).

The above comparison suggests that even considering the different detection limit of the observations and the slightly different approach to estimating the intra-group diffuse light, the IGL estimate for the three groups analysed in this work is consistent with previous values for groups of galaxies of comparable virial mass. Values also agree with fractions of ICL quoted in the literature, which range from 10 to 40% going from groups to clusters (e.g. Feldmeier et al. 2004; Zibetti et al. 2005; McGee & Balogh 2010; Toledo et al. 2011).

The fraction of diffuse light in groups and clusters predicted from numerical simulations also spans the same range of values. Predictions from Sommer-Larsen (2006) are ~12−45%, while more recently Contini et al. (2014) found ~10−40%. The amount of ICL depends on the formation mechanisms. Between approximately 5 and 25% of the diffuse light comes from the infalling galaxies in the potential well of BCGs (or BGGs) during the mass assembly history. Theoretical studies predict that the bulk of the ICL is produced by the most massive satellite galaxies, $M \sim 10^{10-11} M_{\odot}$ (Purcell et al. 2007; Contini et al. 2014; Martel et al. 2012). The contribution to the diffuse light from lower-mass galaxies ($M \leq 10^9 M_{\odot}$) is very little, even though they are more numerous. Therefore, the low amount of IGL detected in the IC 1459 group might be connected to the absence of a galaxy of comparable mass that is interacting with the BGG (see Table 4).

### 6.4. HI distribution versus diffuse light

In this section, for the three groups studied in this work, we aim to compare the HI distribution around the group members and in the intra-group space with the location of the detected LSB features. The HI distribution in the NGC 5018 group and in NGC 1533 triplet results from the ongoing tidal interactions between group members, which are stripping the cold gas from the LTGs (Spavone et al. 2018; Cattapan et al. 2019). The debris from tidal stripping is located in the outskirts of the BGGs, namely NGC 5018 and NGC 1533, in the form of arc-like structures or extended tails. From the deep VEGAS data, we found the optical counterpart for some of the intra-group HI features, at very faint levels $\mu_g \simeq 28-30$ mag arcsec$^{-2}$.

The IC 1459 group shows a different HI distribution. The HI is mainly associated with the group members and it follows the distribution of galaxies along a thick filament in the north–south direction (Kilborn et al. 2009; Saponara et al. 2018). In addition, Fig. 1 shows that there are few HI over-densities that seem not to be associated at any optical feature. The most prominent are close to IC 1459, on the SE and on the NE side. As pointed out in Sect. 4.4, the SE over-density might be associated with the stellar faint tail detected to the south of IC 1459, and linked to the ongoing interaction involving IC 5264 and ESO 406−27 (Saponara et al. 2018; Oosterloo et al. 2018).

A clear difference between the IC 1459 group and the other two groups, NGC 5018 and NGC 1533, is also seen when comparing the IGL component with the total HI mass of the group (i.e. galaxies and intragroup HI). The fraction of IGL light decreases as the HI mass increases; see Fig. 9 (lower panel) and Table 7. Figure 9 suggests that this trend, that is, a lower amount of intra-cluster diffuse light is found in groups with a higher HI gas content, seems also confirmed for other groups of galaxies (with available HI and IGL measurements).

To conclude, by correlating the HI distribution and content with the LSB features and IGL amount, the IC 1459 group seems to be in a different evolutionary phase with respect to the NGC 5018 and NGC 1533 groups. The low amount of IGL, the large HI content, and its regular distribution might indicate that the IC 1459 group is still assembling. This would be in agreement with Saponara et al. (2018), who suggested that given the small HI velocity gradient in the south–southeast direction of IC 1459, in combination with the high number of gas-rich members and low velocity dispersion, the group could be in the first stage of evolution.

## 7. Summary and conclusions

Here, we present and analyse new deep imaging data from the VEGAS survey for the galaxy group IC 1459. The VST mosaics in $g$, $r$, and $i$ bands cover the whole group extension over an area of $1 \times 2$ square degrees. We compare the properties of this group with those of another two low-density systems from VEGAS with similar virial masses: the NGC 5018 group and the NGC 1533 triplet. The NGC 5018 and NGC 1533 groups have similar environments: they have the same number of large galaxies and of ETGs, their HI masses are of the same order of magnitude, and their galaxies are closer in projection to each other. On the contrary, the IC 1459 group is a richer environment with nine bright galaxies of which seven are LTGs; it has a total HI mass of $\sim 10^{10}\,M_\odot$, and its galaxies are located in projection along a filamentary structure of $2°$ in length.

The goal of this study is to investigate low-density environments that remain unexplored at the faintest surface brightness levels where the stellar envelope in the galaxy outskirts and the intra-group light start to dominate. Taking advantage of the deep imaging from VEGAS, the main goal is to address the mass assembly history of the group and its members. This is done by studying (i) the structure of the BGG outskirts, where the tracers of the ongoing accretion (i.e. tidal tails, stellar streams, and shells) can be detected; (ii) the azimuthally averaged surface-brightness radial profile, in order to estimate the accreted stellar mass component; and (iii) the amount of IGL and its distribution. The main properties listed above were correlated with the HI gas mass and distribution. The main results of this work are the following.

1. In the outskirts of IC 1459, which is the BGG of the group, we detect several LSB features in the surface brightness level $25 \leq \mu_g \leq 27$ mag arcsec$^{-2}$. These are shells with red colours in the NE side and two faint and bluer tails to the south (see Fig. 2), which appear to be signs of interaction and accretion in the galaxy stellar halo. Same features are detected in the BGG of another group from the VEGAS sample, NGC 1533, from Cattapan et al. (2019). Alternatively, in the NGC 5018 group a prominent and very extended tidal tail was found, and the outskirts of the BGG are characterised by several stellar streams (Spavone et al. 2018).

2. Like in NGC 5018 and NGC 1533, the azimuthally averaged surface brightness profiles show an extended exponential envelope down to $\mu_g \sim 29$ mag arcsec$^{-2}$ and out to about $9R_e$ (see Fig. 3). By fitting the light distribution, we estimate that the accreted stellar mass in this galaxy is 87%, which is similar to the values derived for NGC 5018 and NGC 1533 (92% and 78%, respectively) and to those of galaxies with comparable total stellar mass in other groups or clusters of galaxies (see Fig. 7).

3. The IC 1459 group has a very low (∼2%) fraction of IGL compared to NGC 5018 and NGC 1533, consistently with its small ETG/LTG ratio and high levels of HI (see Fig. 9).

The above results suggest that the three groups are in a different phase of mass assembly. The filamentary distribution of galaxies in IC 1459, where the HI gas is still associated with the seven LTGs, and the very low amount of IGL are an indication that there were a few minor interactions between the group members and the BGG, which generated the shells and tidal tails detected in the outskirts of IC 1459 (also probably related to the HI over-density observed in the same regions). According to simulations (Mancillas et al. 2019), this would have happened in the last 4 Gyr, which is the survival time of such features. On the contrary, in both NGC 5018 and NGC 1533 groups, many more interactions have happened in their formation history, which have induced gas-depletion by ram pressure stripping and have produced the higher amount of IGL and the disturbed HI distribution; this latter clearly traces the ongoing interaction between some group members (Cattapan et al. 2019; Spavone et al. 2018). Moreover, the HI distribution is related to the environment and to the interaction history of the galaxies. Typically, in interacting or merging galaxies in groups, the HI is located along tails, streams, and bridges, indicating that these structures are formed by tidal stripping (Bekki et al. 2005; Kilborn et al. 2009).

The above scenario is consistent with the NGC 5018 and NGC 1533 groups being at a different evolutionary stage from that of IC 1459. The two former groups have a higher ETG/LTG ratio with respect to that of IC 1459. A larger amount of IGL is expected for more evolved systems with higher ETG/LTG ratios (Da Rocha et al. 2008). The CMDs also confirm that the NGC 5018 and NGC 1533 groups are more evolved systems than

the IC 1549 group, since almost all of their group members are approaching the red sequence. Alternatively, most of the members of the IC 1459 group are still in the region of active and star forming galaxies (see Fig. 6).

In conclusion, this work shows that the structure of the outer envelope of BCGs (i.e. the signatures of past mergers and tidal interactions), the IGL component, and the amount and distribution of HI may be used as indicators of the evolutionary stage and mass assembly of galaxy groups. We plan to perform the analysis presented in this work on a larger group sample from the VEGAS project in the next two years.

# References

Amorisco, N. C. 2017, MNRAS, 464, 2882

Arnaboldi, M., Ventimiglia, G., Iodice, E., Gerhard, O., & Coccato, L. 2012, A&A, 545, A37

Bekki, K., Koribalski, B. S., Ryder, S. D., & Couch, W. J. 2005, MNRAS, 357, L21

Bender, R., Kormendy, J., Cornell, M. E., & Fisher, D. B. 2015, ApJ, 807, 56

Borthakur, S., Yun, M. S., & Verdes-Montenegro, L. 2010, ApJ, 710, 385

Bower, R. G., & Balogh, M. L. 2004, in Clusters of Galaxies: Probes of Cosmological Structure and Galaxy Evolution, eds. J. S. Mulchaey, A. Dressler, & A. Oemler, 325

Brough, S., Forbes, D. A., Kilborn, V. A., & Couch, W. 2006, MNRAS, 370, 1223

Buta, R. 1995, ApJS, 96, 39

Capaccioli, M., Spavone, M., Grado, A., et al. 2015, A&A, 581, A10

Cattapan, A., Spavone, M., Iodice, E., et al. 2019, ApJ, 874, 130

Contini, E., De Lucia, G., Villalobos, Á., & Borgani, S. 2014, MNRAS, 437, 3787

Cook, B. A., Conroy, C., Pillepich, A., Rodriguez-Gomez, V., & Hernquist, L. 2016, ApJ, 833, 158

Cooper, A. P., Cole, S., Frenk, C. S., et al. 2010, MNRAS, 406, 744

Cooper, A. P., D'Souza, R., Kauffmann, G., et al. 2013, MNRAS, 434, 3348

Cooper, A. P., Parry, O. H., Lowing, B., Cole, S., & Frenk, C. 2015, MNRAS, 454, 3185

Da Rocha, C., & Mendes de Oliveira, C. 2005, MNRAS, 364, 1069

Da Rocha, C., Ziegler, B. L., & Mendes de Oliveira, C. 2008, MNRAS, 388, 1433

Deason, A. J., Belokurov, V., Evans, N. W., & Johnston, K. V. 2013, ApJ, 763, 113

De Lucia, G., Springel, V., White, S. D. M., Croton, D., & Kauffmann, G. 2006, MNRAS, 366, 499

DeMaio, T., Gonzalez, A. H., Zabludoff, A., et al. 2018, MNRAS, 474, 3009

Dénes, H., Kilborn, V. A., & Koribalski, B. S. 2014, MNRAS, 444, 667

de Vaucouleurs, G., de Vaucouleurs, A., Corwin, Jr., H. G., et al. 1991, Third Reference Catalogue of Bright Galaxies

Donzelli, C. J., Muriel, H., & Madrid, J. P. 2011, ApJS, 195, 15

D'Souza, R., Kauffman, G., Wang, J., & Vegetti, S. 2014, MNRAS, 443, 1433

Duc, P. A. 2017, in Formation and Evolution of Galaxy Outskirts, eds. A. Gil de Paz, J. H. Knapen, & J. C. Lee, IAU Symp., 321, 180

Duc, P.-A., Cuillandre, J.-C., Karabal, E., et al. 2015, MNRAS, 446, 120

Eskridge, P. B., Frogel, J. A., Pogge, R. W., et al. 2002, ApJS, 143, 73

Feldmeier, J., Mihos, C., Morrison, H., & Harding, P. 2004, Am. Astron. Soc. Meet. Abstr., 205, 146.01

Ferrarese, L., Côté, P., Cuillandre, J.-C., et al. 2012, ApJS, 200, 4

Firth, P., Evstigneeva, E. A., Jones, J. B., et al. 2006, MNRAS, 372, 1856

Forbes, D. A., Franx, M., & Illingworth, G. D. 1994, ApJ, 428, L49

Forbes, D. A., Reitzel, D. B., & Williger, G. M. 1995, AJ, 109, 1576

Forbes, D. A., Gannon, J., Couch, W. J., et al. 2019, A&A, 626, A66

Franx, M., & Illingworth, G. D. 1988, ApJ, 327, L55

Fujita, Y. 2004, PASJ, 56, 29

Gourgoulhon, E., Chamaraux, P., & Fouque, P. 1992, A&A, 255, 69

Grado, A., Capaccioli, M., Limatola, L., & Getman, F. 2012, Mem. Soc. Astron. It. Suppl., 19, 362

Hickson, P., Mendes de Oliveira, C., Huchra, J. P., & Palumbo, G. G. 1992, ApJ, 399, 353

Huang, S., Ho, L. C., Peng, C. Y., Li, Z.-Y., & Barth, A. J. 2013, ApJ, 766, 47

Iodice, E., Capaccioli, M., Grado, A., et al. 2016, ApJ, 820, 42

Iodice, E., Spavone, M., Capaccioli, M., et al. 2017a, ApJ, 839, 21

Iodice, E., Spavone, M., Cantiello, M., et al. 2017b, ApJ, 851, 75

Iodice, E., Spavone, M., Capaccioli, M., et al. 2019, A&A, 623, A1

Kilborn, V. A., Koribalski, B. S., Forbes, D. A., Barnes, D. G., & Musgrave, R. C. 2005, MNRAS, 356, 77

Kilborn, V. A., Forbes, D. A., Barnes, D. G., et al. 2009, MNRAS, 400, 1962

Kim, D. W., Guhathakurta, P., van Gorkom, J. H., Jura, M., & Knapp, G. R. 1988, ApJ, 330, 684

La Barbera, F., Ferreras, I., de Carvalho, R. R., et al. 2012, MNRAS, 426, 2300

Malin, D. F. 1985, in Food for the Photometrists – Faint Galaxies Revealed, ed. J. L. Nieto, 27

Mancillas, B., Duc, P. A., Combes, F., et al. 2019, A&A, 632, A122

Martel, H., Barai, P., & Brito, W. 2012, ApJ, 757, 48

Mazzei, P., Marino, A., & Rampazzo, R. 2014, ApJ, 782, 53

McFarland, J. P., Verdoes-Kleijn, G., Sikkema, G., et al. 2013, Exp. Astron., 35, 45

McGee, S. L., & Balogh, M. L. 2010, MNRAS, 405, 2069

Merritt, A., van Dokkum, P., Danieli, S., et al. 2016, ApJ, 833, 168

Mihos, C. 2015, IAU Gen. Assem., 22, 2247903

Mihos, J. C., Harding, P., Feldmeier, J. J., et al. 2017, ApJ, 834, 16

Miles, T. A., Raychaudhury, S., Forbes, D. A., et al. 2004, MNRAS, 355, 785

Monachesi, A., Gómez, F. A., Grand, R. J. J., et al. 2019, MNRAS, 485, 2589

Muñoz, R. P., Eigenthaler, P., Puzia, T. H., et al. 2015, ApJ, 813, L15

Nishiura, S., Murayama, T., Shimada, M., et al. 2000, AJ, 120, 2355

Oosterloo, T. A., Zhang, M. L., Lucero, D. M., & Carignan, C. 2018, ArXiv e-prints, unpublished [arXiv:1803.08263]

Oser, L., Ostriker, J. P., Naab, T., Johansson, P. H., & Burkert, A. 2010, ApJ, 725, 2312

Osmond, J. P. F., & Ponman, T. J. 2004, MNRAS, 350, 1511

Pillepich, A., Nelson, D., Hernquist, L., et al. 2018, MNRAS, 475, 648

Pop, A.-R., Pillepich, A., Amorisco, N. C., & Hernquist, L. 2018, MNRAS, 480, 1715

Prichard, L. J., Vaughan, S. P., & Davies, R. L. 2019, MNRAS, 488, 1679

Purcell, C. W., Bullock, J. S., & Zentner, A. R. 2007, ApJ, 666, 20

Ribeiro, A. L. B., de Carvalho, R. R., Capelato, H. V., & Zepf, S. E. 1998, ApJ, 497, 72

Ricciardelli, E., Vazdekis, A., Cenarro, A. J., & Falcón-Barroso, J. 2012, MNRAS, 424, 172

Rudick, C. S., Mihos, J. C., Frey, L. H., & McBride, C. K. 2009, ApJ, 699, 1518

Rudick, C. S., Mihos, J. C., & McBride, C. K. 2011, ApJ, 732, 48

Ryder, S. D., Purcell, G., Davis, D., & Andersen, V. 1997, PASA, 14, 81

Ryder, S. D., Purcell, G., Andersen, V., & Davis, D. 2000, in Dynamics of Galaxies: from the Early Universe to the Present, eds. F. Combes, G. A. Mamon, & V. Charmandaris, ASP Conf. Ser., 197, 405

Saponara, J., Koribalski, B. S., Benaglia, P., & Fernández López, M. 2018, MNRAS, 473, 3358

Schipani, P., Noethe, L., Arcidiacono, C., et al. 2012, J. Opt. Soc. Am. A, 29, 1359

Seigar, M. S., Graham, A. W., & Jerjen, H. 2007, MNRAS, 378, 1575

Selim, I., & Iqbal, N. 2008, Turk. J. Phys., 32, 133

Serra, P., Koribalski, B., Kilborn, V., et al. 2015, MNRAS, 452, 2680

Sommer-Larsen, J. 2006, MNRAS, 369, 958

Spavone, M., Capaccioli, M., Napolitano, N. R., et al. 2017a, The Messenger, 170, 34

Spavone, M., Capaccioli, M., Napolitano, N. R., et al. 2017b, A&A, 603, A38

Spavone, M., Iodice, E., Capaccioli, M., et al. 2018, ApJ, 864, 149

Thilker, D. A., Bianchi, L., Meurer, G., et al. 2007, ApJS, 173, 538

Tingay, S. J., & Edwards, P. G. 2015, MNRAS, 448, 252

Toledo, I., Melnick, J., Selman, F., et al. 2011, MNRAS, 414, 602

van Dokkum, P. G., Abraham, R., & Merritt, A. 2014, ApJ, 782, L24

Vazdekis, A., Ricciardelli, E., Cenarro, A. J., et al. 2012, MNRAS, 424, 157

Venhola, A., Peletier, R., Laurikainen, E., et al. 2018, A&A, 620, A165

White, P. M., Bothun, G., Guerrero, M. A., West, M. J., & Barkhouse, W. A. 2003, ApJ, 585, 739

Willman, B., Governato, F., Wadsley, J., & Quinn, T. 2004, MNRAS, 355, 159

Wyder, T. K., Martin, D. C., Schiminovich, D., et al. 2007, ApJS, 173, 293

Zibetti, S., White, S. D. M., Schneider, D. P., & Brinkmann, J. 2005, MNRAS, 358, 949

# Appendix A: Surface photometry of the IC 1459 group

## A.1. IC 5270

This late-type barred spiral galaxy is the northernmost galaxy of the group, lying at a projected distance of 37′.3 from IC 1459. From the VST images (Fig. B.1) there is not a clear optical counterpart for the north–northeast HI asymmetric distribution. The edge-on galaxy inclination does not allow us to investigate the stellar disk asymmetries and bar component.

## A.2. IC 5269

This is a barred lenticular galaxy with an average colour ($g − r = 0.77 ± 0.25$ mag) consistent with the predicted colour of ETGs (La Barbera et al. 2012). It is the forth most massive ($3.32 × 10^{10} M_\odot$) and smallest bright galaxy ($R_{e,g} = 2.70$ kpc) of the group. Its surface brightness profiles present clear evidence for the bulge and stellar disk components. Its colour profile is almost flat outside of the seeing-dominated region. It does not have any associated HI (Fig. B.2).

## A.3. IC 5269B

This is the second closest galaxy in projection to IC 1459 (14′.5). It is the second to least bright, $M_g = −19.60$ mag, and is the least massive, $5.0 × 10^9 M_\odot$, bright galaxy of the group. This galaxy is very inclined with bluer outer regions (Fig. B.3). The HI component is off-centre with respect to the stellar disk; this latter seems to be more elongated in the opposite direction. This could be due to some galaxy–galaxy or galaxy–environment interaction, providing a tidal stripping component and this gas might build up the debris structure around IC 1459.

## A.4. IC 5264

This is a peculiar, very small ($R_{e,g} = 4.05$ kpc), edge-on, early-type spiral. The average colour ($g − r = 0.79 ± 0.06$ mag) is too red for a LTG, but this galaxy is seen in projection in the IC 1459 stellar halo. This could explain why they have a similar $g − r$ average colour. From the VST images (Fig. B.4), we were able to detect the warped structure of the outer stellar envelope and a dust lane in the southeaster side of the stellar disk in agreement with the HI off-centre distribution, which seems to be tangent to the outer envelope of IC 1459 in the eastern direction. Its HI component is faint and is spread in a wide velocity range (Serra et al. 2015). It has been suggested that IC 5264 is the principal donor of HI gas around IC 1459 thanks to a tidal interaction (Saponara et al. 2018).

## A.5. ESO 406−27

This is the bluest ($g − r = 0.34 ± 0.20$ mag) bright galaxy of the group, and has a total stellar mass ($3.2 × 10^9 M_\odot$) one order of magnitude smaller than the other galaxies except for IC 5269B. It is located on the southwest side of IC 1459 at a project distance of 19.5′. It is one of the HI brightest sources with a HI mass of $(4.6 ± 0.9) × 10^9 M_\odot$ (Serra et al. 2015). From Fig. B.5, ESO 406−27 might be interacting both with IC 1459 and NGC 7418. It has a two-spiral-arms pattern which is clearly in the direction of these galaxies, which corresponds to the HI asymmetry. However we do not have enough information yet to form an hypothesis regarding the evolution or interaction scenario between IC 1459, ESO 406−27, and NGC 7418. GALEX data confirms that there are two spiral, UV-bright arms extending from the northeast to the southwest (Thilker et al. 2007).

## A.6. NGC 7418

This is the second brightest ($M_g = −21.98$ mag), massive ($10.87 × 10^{10} M_\odot$), and biggest ($R_{e,g} = 21.72$ kpc), galaxy of the group and is at a projected distance of 34′.8 from IC 1459 in the southern region of the group. This late-type spiral has a very asymmetric stellar disk in the northwest direction. It has a weak optical bar seen in the surface brightness profile rather than in the optical colour composite image (Fig. B.6). It seems to be stronger in $H$ band imaging (Eskridge et al. 2002). The spiral arms are well defined in the inner regions, becoming bluer and smoothed in the outer parts. As explored by Serra et al. (2015) and Oosterloo et al. (2018), the complex HI tidal features elongated from the north region of the group to NGC 7418 seem to be the result of the first tidal galaxy–galaxy and galaxy–environment interactions that have occurred in the BGG neighbourhood.

## A.7. NGC 7421

This is a late-type barred spiral with an inner resonance ring (Buta 1995). It has the smallest relative velocity ($v_{rel} = −9.59$ km s$^{-1}$) with respect to IC 1459. It is the third smallest, $R_{e,g} = 5.26$ kpc, and least massive ($2.44 × 10^{10} M_\odot$) galaxy. The colour composite VST image (Fig. B.7, left panel) shows the small inner bar and the southeast light asymmetries due to the spiral arms and the outer envelope of the galaxy that are consistent with the off-centre HI disk. The recent study made by Serra et al. (2015) showed that the HI asymmetry in the opposite direction of the star-forming optical disk might be the signature of ram pressure stripping. According to Dénes et al. (2014), this galaxy is a HI-deficient galaxy, $\mathcal{M}_{HI} = (1.1 ± 0.3) × 10^9 M_\odot$ (Serra et al. 2015). However, according to Ryder et al. (1997, 2000), the tenuous hot intragroup medium is not able to produce a significant ram pressure stripping and hence tidal interactions might produce a couple of tails. The conclusion is that the galaxy had a previous tidal interaction, maybe with NGC 7418, which affected the stellar disk and the HI gas, and a subsequent weak ram pressure stripping, as was the case for IC 5273, which dislocated the HI gas.

## A.8. IC 5273

This late-type barred spiral is the third brightest galaxy of the group ($M_g = −21.59$ mag). It is the most distant galaxy in projection from IC 1459 (79′.2), and it has the largest relative velocity to IC 1459 ($v_{rel} = −509 ± 17$ km s$^{-1}$). The bar is clearly visible (Fig. B.8) both in the colour composite image and in the surface-brightness radial profile ($6'' ≤ R ≤ 40''$). The average colours are $g − r = 0.54$ mag and $g − i = 1.05$ mag, and the colour profiles have a bluer decline for $R > 3''$. It is also one of the brightest sources in ASKAP HI, $\mathcal{M}_{HI} = (5.4 ± 1.1) × 10^9 M_\odot$ (Serra et al. 2015). The HI gas and stellar disk are off-centre, and the HI distribution has a southeast asymmetry opposite to the direction of IC 1459. The galaxy could have suffered some interactions with the environment or ram pressure stripping, as for NGC 7421 (Serra et al. 2015).

## Appendix B: Surface photometry

For each galaxy of the IC 1459 group, we report the results of the surface photometry, from Figs. B.1 to B.8. A colour composite image (red channel for *i* band, green channel for *r* band, and blue channel for *g* band; left panel) is shown that was extracted from the VST mosaic around the galaxy, with the HI map from the KAT−7 observations (cyan contours). We also report the azimuthally averaged surface-brightness radial profile plotted in logarithmic scale as a function of the semi-major axis (middle panel), and the azimuthally averaged extinction-corrected $g − r$, $r−i$, and $g−i$ colour profile as a function of the logarithmic semi-major axis (right panel). These plots are derived by the isophote fit from $g$ (blue dots), $r$ band (orange dots), and $i$ band (red dots) VST images.
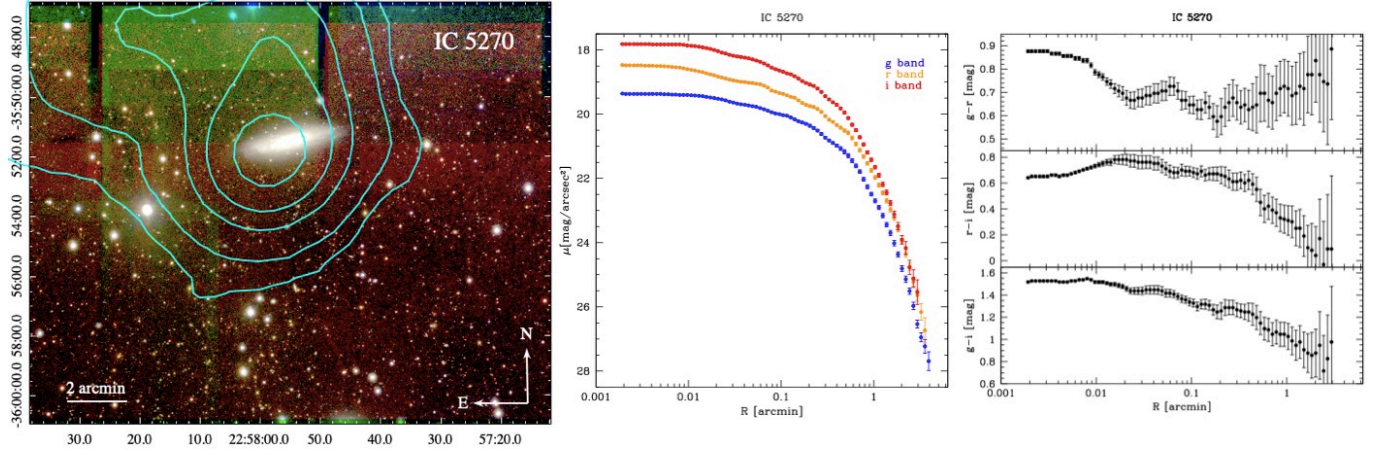


**Fig. B.1.** *Left panel*: colour composite image of IC 5270 with north at the top and east to the left. The right ascension and declination (J2000) are given in the horizontal and vertical axis of the field of view, respectively. The HI contours levels (white contours) are 1, 2.5, 7.5, 12.5, and $20 \times 10^{19}$ cm$^{-2}$. The white arrow indicates the direction of the BGG, IC 1459, with respect to the galaxy. *Middle panel*: $g$, $r$, and $i$ band azimuthally averaged surface-brightness radial profile. *Right panel*: azimuthally averaged extinction-corrected $g − r$, $r − i$, and $g − i$ colour profiles.
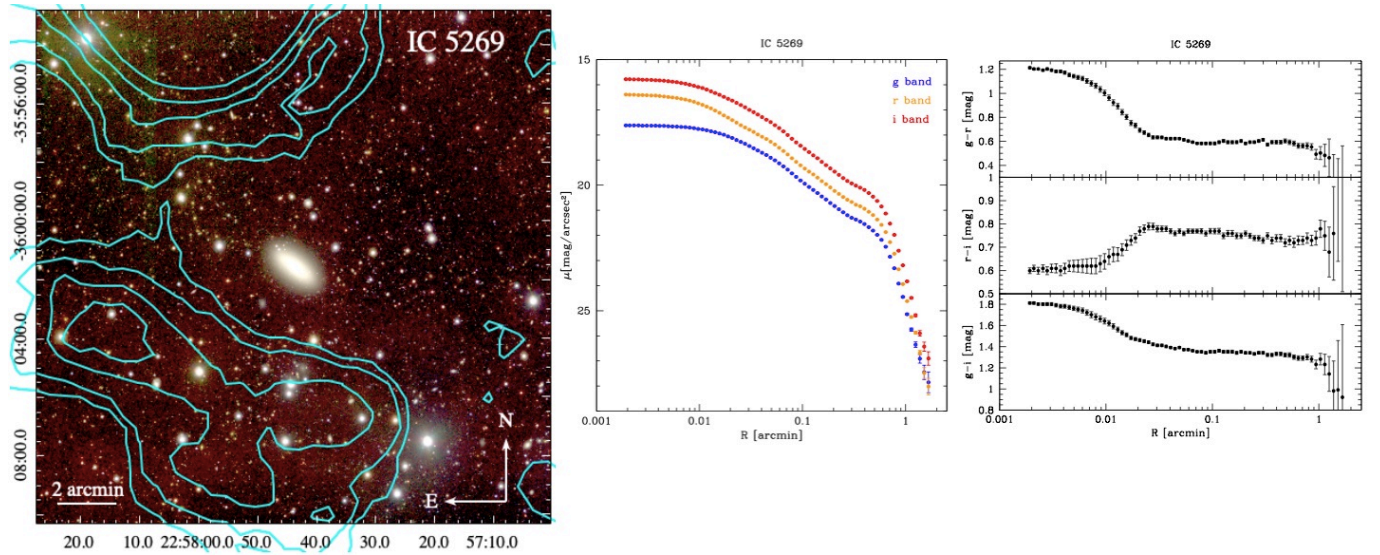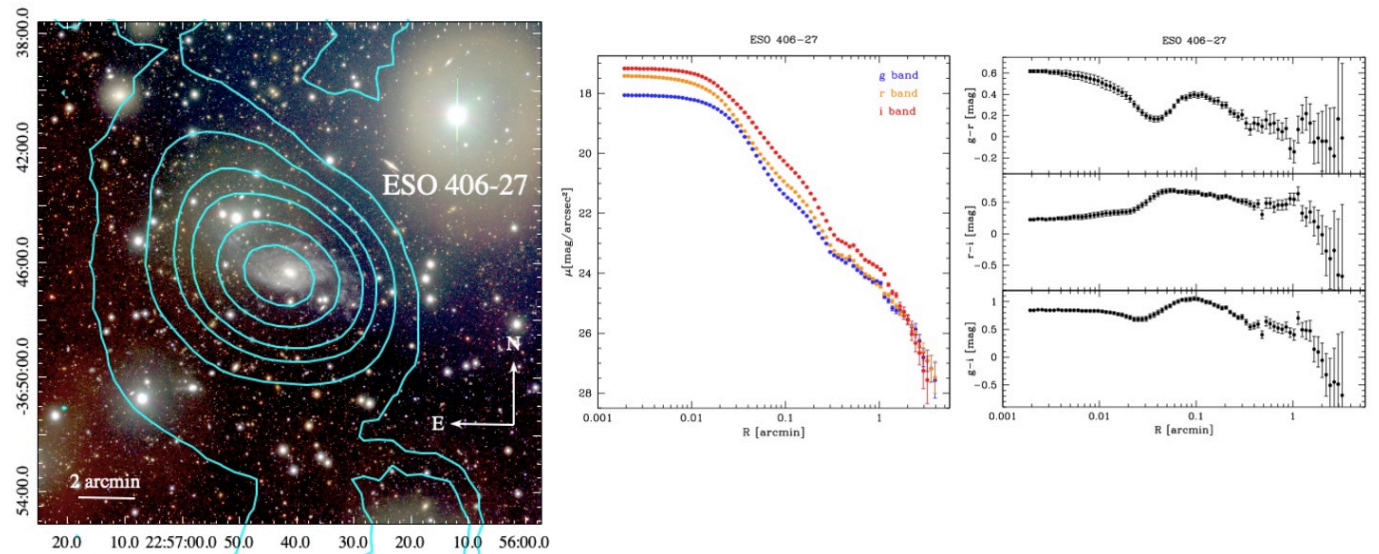


**Fig. B.2.** Same as Fig. B.1 but for IC 5269. The HI contour levels are 0.25, 0.5, 1, 1.5, and $2.5 \times 10^{19}$ cm$^{-2}$.
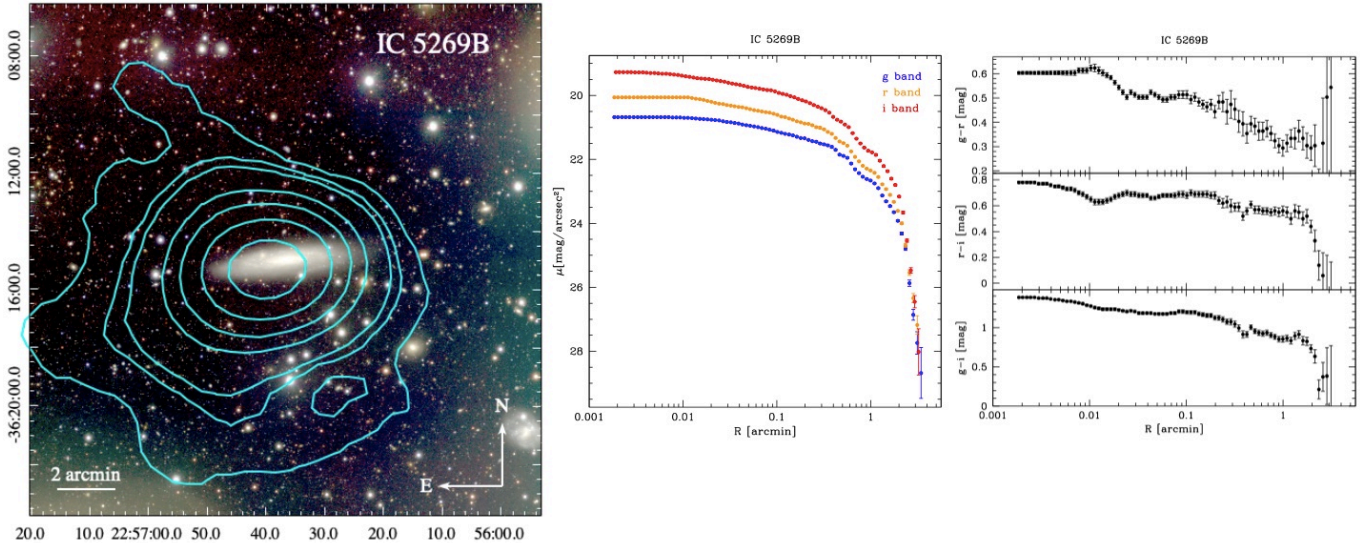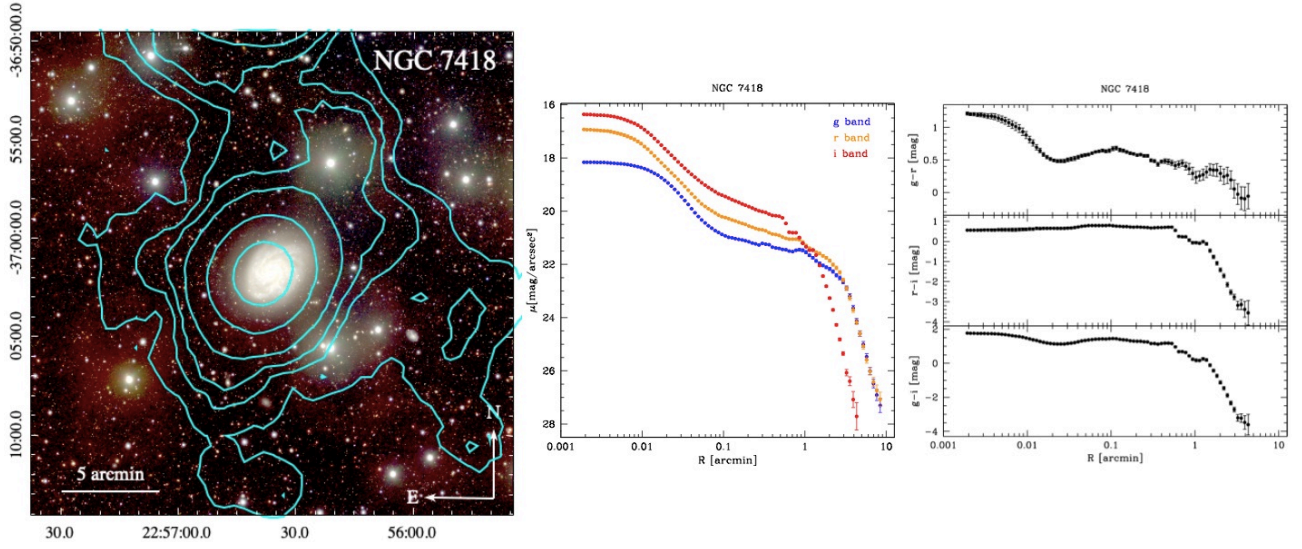
**Fig. B.3.** Same as Fig. B.1 but for IC 5269B. The HI contour levels are 0.25, 1, 2.5, 7.5, 12.5, 20, and $30 \times 10^{19}$ cm$^{-2}$.
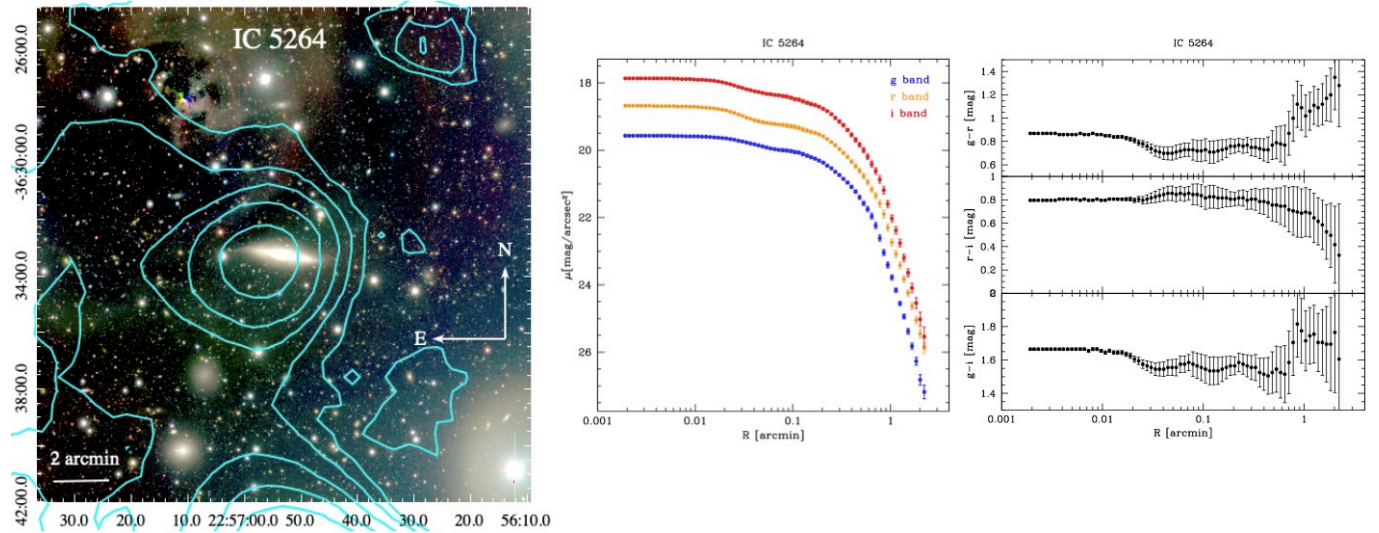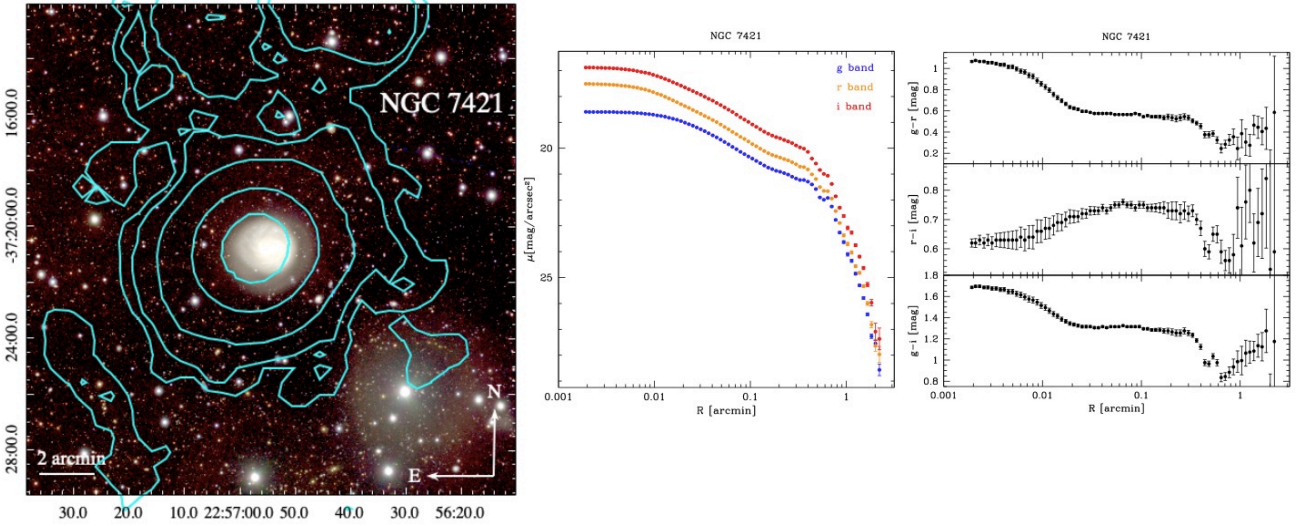


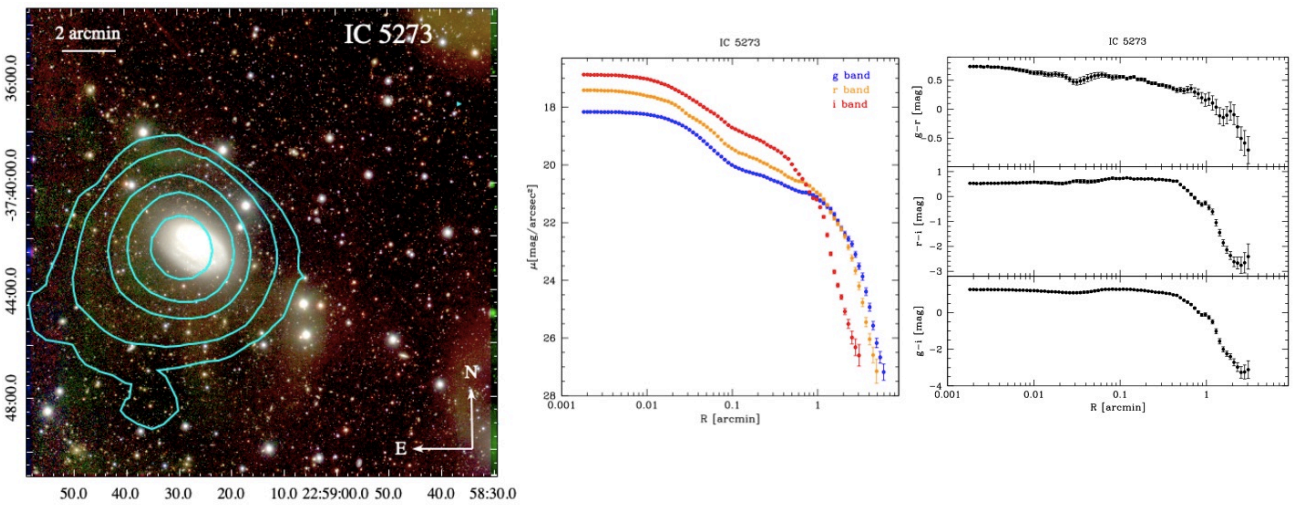**Fig. B.4.** Same as Fig. B.1 but for IC 5264. The HI contour levels are 0.25, 1, 2.5, 5, and $10 \times 10^{19}$ cm$^{-2}$.



**Fig. B.5.** Same as Fig. B.1 but for ESO 406-27. The HI contour levels are 1.5, 5, 10, 15, 25, and $35 \times 10^{19}$ cm$^{-2}$.

**Fig. B.6.** Same as Fig. B.1 but for NGC 7418. The HI contour levels are 0.5, 1.5, 2.5, 5, 15, and $35 \times 10^{19}$ cm$^{-2}$.



**Fig. B.7.** Same as Fig. B.1 but for NGC 7421. The HI contour levels are 0.25, 0.5, 1.5, 5, and $10 \times 10^{19}$ cm$^{-2}$.



**Fig. B.8.** Same as Fig. B.1 but for IC 5273. The HI contour levels are 1, 2.5, 7.5, 12.5, and $20 \times 10^{19}$ cm$^{-2}$.